Detection of non-thermal X-ray emission in the lobes and jets of Cygnus A

M. N. de Vries[1] ⋆, M. W. Wise[2,1], D. Huppenkothen[3], P. E. J. Nulsen[4], B. Snios[4],
M. J. Hardcastle[5], M. Birkinshaw[6], D. M. Worrall[6], R. T. Duffy[6], and B. R. McNamara[7,8]

[1] *Astronomical Institute "Anton Pannekoek", University of Amsterdam, Science Park 904, 1098 XH Amsterdam, The Netherlands*
[2] *ASTRON, Netherlands Institute for Radio Astronomy, Postbus 2, 7990 AA, Dwingeloo, The Netherlands*
[3] *Department of Astronomy, University of Washington, 3910 15th Ave NE, Seattle, WA 98195*
[4] *Harvard-Smithsonian Center for Astrophysics, 60 Garden Street, Cambridge, MA 02138*
[5] *School of Physics, Astronomy and Mathematics, University of Hertfordshire, College Lane, Hatfield AL10 9AB, UK*
[6] *HH Wills Physics Laboratory, University of Bristol, Tyndall Avenue, Bristol, BS8 1TL, UK*
[7] *Department of Physics and Astronomy, University of Waterloo, 200 University Ave W, Waterloo, ON N2L 3G1, Canada*
[8] *Perimeter Institute for Theoretical Physics, 31 Caroline St. North, Waterloo, ON N2L 2Y5, Canada*

ABSTRACT

We present a spectral analysis of the lobes and X-ray jets of Cygnus A, using more than 2 Ms of *Chandra* observations. The X-ray jets are misaligned with the radio jets and significantly wider. We detect non-thermal emission components in both lobes and jets. For the eastern lobe and jet, we find 1 keV flux densities of 71^{+10}_{-10} nJy and 24^{+4}_{-4} nJy, and photon indices of $1.72^{+0.03}_{-0.03}$ and $1.64^{+0.04}_{-0.04}$ respectively. For the western lobe and jet, we find flux densities of 50^{+12}_{-13} nJy and 13^{+5}_{-5} nJy, and photon indices of $1.97^{+0.23}_{-0.10}$ and $1.86^{+0.18}_{-0.12}$ respectively. Using these results, we modeled the electron energy distributions of the lobes as broken power laws with age breaks. We find that a significant population of non-radiating particles is required to account for the total pressure of the eastern lobe. In the western lobe, no such population is required and the low energy cutoff to the electron distribution there needs to be raised to obtain pressures consistent with observations. This discrepancy is a consequence of the differing X-ray photon indices, which may indicate that the turnover in the inverse-Compton spectrum of the western lobe is at lower energies than in the eastern lobe. We modeled the emission from both jets as inverse-Compton emission. There is a narrow region of parameter space for which the X-ray jet can be a relic of an earlier active phase, although lack of knowledge about the jet's electron distribution and particle content makes the modelling uncertain.

Key words: X-rays:galaxies - galaxies:individual:Cygnus A - galaxies:jets

1 INTRODUCTION

Cygnus A (hereafter Cyg A) is a FRII radio galaxy (Fanaroff & Riley 1974). Its extreme radio brightness (Stockton & Ridgway 1996) made it one of the first objects of such type to be discovered. Radio observations show extended, plume-like lobe structures of synchrotron-emitting plasma, as well as jets extending to the east and west of the AGN, which terminate in bright hotspots where the jets are driving shocks into the surrounding intracluster medium (ICM) (Carilli et al. 1988, 1991, 1994). In the X-ray, these shocks are observed as a sharp brightness edge ahead of the hotspots, and are also referred to as the cocoon shocks (Wilson et al. 2006).

Inverse-Compton (IC) emission has been detected in the lobes and hotspots of many FRII sources, (e.g Hardcastle et al. 2002;

Konar et al. 2009). There are different names for the IC emission depending on the seed photons that are scattered. The types usually considered are IC scattering of the Cosmic Microwave Background (IC/CMB) (Harris & Grindlay 1979), of synchrotron photons (synchrotron self-Compton, or SSC), or of infrared photons from the AGN (Brunetti et al. 1997). Because the IC spectrum is directly linked to the electron energy distribution, it probes low-energy electrons in the lobes. The combination of the X-ray IC spectrum, the radio synchrotron spectrum and the total pressure then provide constraints on the distribution of electron energies and the magnetic field strength in the lobes. For FRII sources it has been shown that most sources have overpressured lobes with electron-dominated internal energies (Ineson et al. 2017).

It is common to assume equipartition to model the lobe energy density, especially for FRI galaxies. Many FRI galaxies show deficits compared to the external pressure that seem to require

⋆ E-mail: m.n.devries@uva.nl (KTS)

a significant quantity of non-radiating particles, such as protons (Morganti et al. 1988; Bîrzan et al. 2004; Hardcastle et al. 2007). This population could be created by entrainment of material by the jets(Croston et al. 2008; Croston & Hardcastle 2014).

Detecting IC emission from the lobes in Cyg A has proven challenging as a result of the rich cluster environment containing bright, relatively hot thermal emission. Recent work by Wise et al. (in prep.) shows that the ICM around and in front of the western lobe is significantly hotter than on the eastern side, and shows more temperature variation. This temperature structure could be a signature of earlier cycles of AGN activity, a shock generated by the early phase merger with the northwestern subcluster (Cygnus NW), or some combination of the two.

Previous work has claimed detection of non-thermal emission in the Cyg A lobes (Hardcastle & Croston 2010; Yaji et al. 2010). The non-thermal lobe fluxes in these papers are consistent with each other, although the errors are large. The result shows that Cyg A may be different from other FRII galaxies in that the electron population is not energetically dominant, and that the jet entrainment model for FRI radio galaxies may be important for Cyg A as well (Hardcastle & Croston 2010).

The wide, linear features extending east and west of the AGN in the X-ray are generally assumed to be X-ray analogues of the radio jets. Although the nature of these features is partially unclear, we will refer to them throughout this paper as the X-ray jets. Dreher et al. (1987) derived an upper limit to the thermal electron density in the lobes of Cyg A, using Faraday rotation measurements. These limits are difficult to reconcile with a thermal model for the jet emission, as shown in Steenbrugge et al. (2008).

If the X-ray jets are non-thermal in origin, it is unclear which non-thermal emission mechanism would produce extended X-ray jets on kiloparsec scales. Generally, two different models have been invoked for these kinds of jets. The first model is the boosted IC/CMB model (Tavecchio et al. 2000; Celotti et al. 2001). In this model, high bulk Lorentz factors at small angles to the line of sight Doppler boost the upscattered photons enough to produce detectable X-ray emission. The model has been applied to quasar jets. However, in Cyg A the eastern, receding jet appears to be brighter in X-rays than the western, approaching jet. Doppler boosting would only have the opposite effect on the eastern jet, and increase the difference in intrinsic emissivities between the two jets. Therefore, we consider the boosted IC/CMB model unlikely to apply to Cyg A.

The synchrotron model is often proposed as an alternative to the IC/CMB model. X-ray synchrotron emission requires electrons with very high Lorentz factors. Because the lifetime of X-ray synchrotron-emitting electrons is only on the order of tens to hundreds of years, the electrons require *in situ* acceleration. Electron re-acceleration is achieved through shocks, which happen locally in jet knots. A synchrotron jet model can therefore explain more naturally the knottiness seen in some of the extended X-ray jets (Hardcastle et al. 2016). In synchrotron models, many systems with multi-wavelength observations show that the radio, optical/IR, and X-ray data cannot be explained with a single electron energy distribution, which implies the existence of a second, more energetic component (e.g. Jester et al. 2006; Hardcastle 2006; Uchiyama et al. 2006). It is unclear how a second electron energy distribution could be created.

A few morphological differences make the Cyg A jets unlike most other radio/X-ray jet systems. The most obvious difference is that the X-ray jets are at least 4-6 times wider than the radio jet, extending several arcseconds in width. An extended X-ray jet

structure has been observed in the quasar PKS 1055+201 (Schwartz et al. 2006). Moreover, the X-ray jets and radio jets are misaligned (Steenbrugge & Blundell 2008). While aligned with each other close to the AGN, midway to the lobe the X-ray jets extend relatively straight towards the brightest hotspots, while the radio jets bend southwards to the fainter hotspots. Based on these morphological differences, Steenbrugge et al. (2008) argue that the Cyg A jets are IC/CMB-emitting relic jets, emitted by an older electron population that was left behind from earlier passage of the radio jet. In this model, when the radio jet changes direction through precession or for some other reason, the electron population of the radio jet expands adiabatically into the medium, reducing electron energies to the range required to produce IC/CMB X-rays. This would explain the spatial misalignment of the jets, as well as the greater width of the X-ray jet. The IC relic jet model could also explain the brightness difference between the two jets through the difference in light travel time. The Cyg A cocoon is inclined at ∼ 55 degrees to our line of sight (Vestergaard & Barthel 1993). This means light from the eastern hotspot has an additional light travel time of ∼ 2×10^5 yrs. The difference in light travel time could explain the relative faintness of the western jet: it has had more time to fade and expand.

However, the question remains how this relic X-ray jet could exist long enough as a linear feature for us to observe it. If the adiabatic expansion is too fast, the jets would not be observed as a linear feature. Moreover, a fast expansion of the jet would shock the material in the lobes. The observed X-ray jet morphology implies that the jets would have to be fairly close to pressure balance with the lobes. Because the jets are brighter than the surrounding lobe, this is difficult to achieve unless the jets and lobes have significantly different electron populations or particle content. Additionally, it is difficult to maintain the observed knotty jet structure as this implies significant local pressure variations. In an expanding relic jet scenario, those pressure variations should smooth out during the expansion.

In this paper we use 1.8 Ms of new *Chandra* observations, combined with 200ks of archival observations, to analyse the emission from the lobes and X-ray jets of Cyg A. Complementary results for the inner gas structure and outer lobe shocks appear in Duffy et al. (2018) and Snios et al. (2018), respectively. We compare different models for the lobe and jet emission and constrain their parameters. With these parameters, we model the energy density of the lobes and test the possibility of an IC relic jet. We show the data and detail the data reduction in section 2. We give an overview of the statistical tools and the models that we used in section 3. We present the results of the statistical analysis in section 4, and discuss their interpretation in section 5. We conclude in section 6.

Throughout this paper, we adopt a cosmology with H_0= 69.3 km s^{-1} Mpc^{-1}, Ω_M = 0.288, and Ω_Λ = 0.712 (Hinshaw et al. 2013). We use a redshift value of z=0.0561 (Stockton et al. 1994). This yields a linear scale of 66 kpc per arcminute and a luminosity distance D_L = 253.2 Mpc for Cyg A. The spectral index α is defined so that flux ∝ $\nu^{-\alpha}$, and related to the X-ray photon index as $\Gamma = 1 + \alpha$.

2   X-RAY OBSERVATIONS AND DATA REDUCTION

2.1   Data reduction

This paper uses nearly all of the Cyg A data available on the *Chandra* archive. This includes 200 ks of previous observations taken between 2000 and 2005, and 2 Ms of recent observations taken between 2015 and 2017. A subset of 200ks of the recent observations

Table 1. Observation log of Chandra Cyg A data used in this paper

ObsID[a]	Date[b]	T_{exp}[c] (ksec)	Pointing[d]	ObsID[a]	Date[b]	T_{exp}[c] (ksec)	Pointing[d]
360*	2000 05 21	34.7	Nucleus	17138	2016 07 25	26.4	W Hotspot
1707*	2000 05 26	9.2	Nucleus	17513	2016 08 15	49.1	Nucleus
6225	2005 02 15	24.3	Nucleus	17516	2016 08 18	49.0	W Hotspot
5831	2005 02 16	50.8	Nucleus	17523	2016 08 31	49.4	E Hotspot
6226	2005 02 19	23.7	Nucleus	17512	2016 09 15	66.9	Nucleus
6250	2005 02 21	7.0	Nucleus	17139	2016 09 16	39.5	W Hotspot
5830	2005 02 22	23.2	Nucleus	17517	2016 09 17	26.7	W Hotspot
6229	2005 02 23	22.8	Nucleus	19888	2016 10 01	19.5	W Hotspot
6228	2005 02 25	16.0	Nucleus	17140	2016 10 02	34.3	W Hotspot
6252	2005 09 07	29.7	Nucleus	17507	2016 11 12	32.4	Nucleus
17530	2015 04 19	21.3	E Hotspot	17520	2016 12 06	26.8	W Hotspot
17650	2015 04 22	28.2	E Hotspot	19956	2016 12 10	54.1	W Hotspot
17144	2015 05 03	49.4	E Hotspot	17514	2016 12 13	49.4	Nucleus
17141	2015 08 01	29.6	E Hotspot	17529	2016 12 15	35.1	E Hotspot
17710	2015 08 07	19.8	E Hotspot	17519	2016 12 19	29.4	W Hotspot
17528	2015 08 30	49.3	E Hotspot	17135	2017 01 20	19.8	Nucleus
17143	2015 09 03	27.1	E Hotspot	17136	2017 01 26	22.2	Nucleus
17524	2015 09 08	23.0	E Hotspot	19996	2017 01 28	28.6	Nucleus
18441	2015 09 14	24.6	E Hotspot	19989	2017 02 12	41.5	Nucleus
17526	2015 09 20	49.4	E Hotspot	17515	2017 03 22	39.0	W Hotspot
17527	2015 10 11	26.8	E Hotspot	20043	2017 03 26	29.3	W Hotspot
18682	2015 10 14	22.8	E Hotspot	20044	2017 03 27	14.6	W Hotspot
18641	2015 10 15	22.4	E Hotspot	17137	2017 03 30	25.2	W Hotspot
18683	2015 10 18	15.6	E Hotspot	17522	2017 04 08	48.6	W Hotspot
17508	2015 10 28	14.9	Nucleus	20059	2017 04 19	23.7	E Hotspot
18688	2015 11 01	34.6	Nucleus	17142	2017 04 20	23.3	E Hotspot
18871	2016 06 13	21.8	Nucleus	17525	2017 04 22	24.7	E Hotspot
17133	2016 06 18	30.2	Nucleus	20063	2017 04 22	25.4	E Hotspot
17510	2016 06 26	37.3	Nucleus	17511	2017 05 10	15.9	Nucleus
17509	2016 07 10	51.2	Nucleus	20077	2017 05 13	27.7	Nucleus
17518	2016 07 16	49.4	W Hotspot	20048	2017 05 19	22.7	E Hotspot
17521	2016 07 20	24.5	W Hotspot	17134	2017 05 20	29.4	Nucleus
18886	2016 07 23	21.5	W Hotspot	20079	2017 05 21	23.8	Nucleus
					Total	2005.3	

[a] The *Chandra* Observation ID number. ObsID's marked with an asterisk indicate ACIS-S observations.
[b] The date of the observation .
[c] The exposure times after filtering for flares.
[d] The aimpoint location of the observation. Three different aimpoints have been used in this data set: the AGN, as well as the western and eastern hotspots.

.

were excluded, as they are pointed at the northwestern subcluster Cyg NW and the filamentary region between the two subclusters. This leaves a total data set of more than 2 Ms. A log of all the observations, with their filtered exposure times and pointings, is shown in Table 1. For an extended review of the full data set and the large scale structure of the system, we refer to Wise et al. (in prep).

Each of these data sets has been reprocessed with `CIAO` 4.9 and `CALDB` 4.7.4 (Fruscione et al. 2006). Before reprocessing the data, we corrected for small astrometric errors caused by *Chandra's* pointing accuracy of around 0.5 arcsec. We followed the procedure described by Snios et al. (2018), briefly summarised here. We chose ObsID 5831 as the reference observation for the high total counts. We then reprojected the event lists of the other ObsID onto the sky frame of ObsID 5831. For each ObsID, we cross-correlated a 0.5 - 7.0 keV 160 x 120 arcsec region around the central AGN with ObsID 5831 to determine the coordinate offset. The coordinate shift was then applied to the event list and aspect solution files with *wcs_update*.

After the astrometry correction, we applied the following `CIAO` processing tools. For each ObsID, a new badpix file was built with *acis_build_badpix*. We applied the latest gain and CTI corrections with *acis_process_events*. We created a new level 2 event file by filtering for good grades (0,2,3,4,6). After that, we filtered for GTIs with the tool *deflare*. Finally, we identified readout streaks with *acis_streak_map* and filtered them out.

The background event files were created from the ACIS blank sky event files. The backgrounds were imported from the calibration database with the tool *acis_bkgrnd_lookup*, and reprojected. The backgrounds were scaled to the data by using the counts between 10.0 - 12.0 keV. The event files and backgrounds were all separately reprojected and added together to form a merged counts image and a merged background map. We show the merged 0.5 - 7.0 keV counts image in Fig. 1.

As well as the X-ray data, we have used two radio maps of the system: a 4.5 GHz VLA radio map from Perley et al. (1984), and 150 MHz LOFAR radio map from McKean et al. (2016). The radio maps
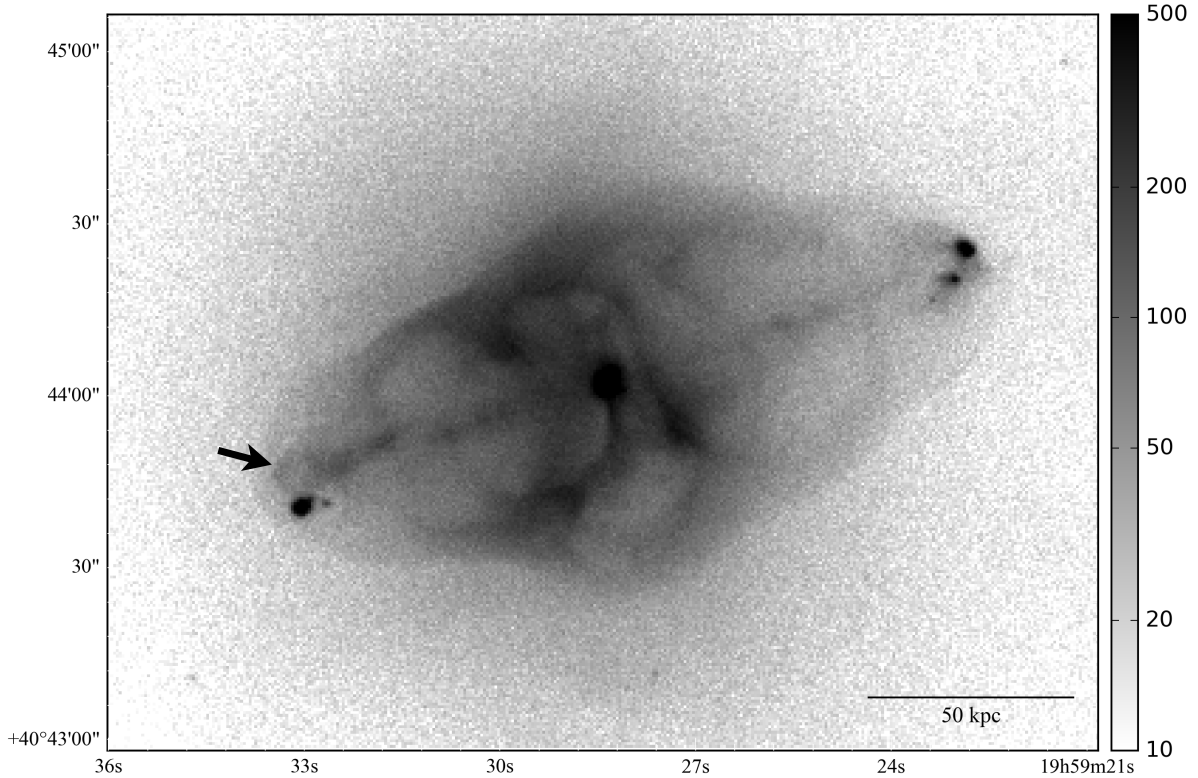
Figure 1. The merged 0.5 - 7.0 keV counts image Cyg A, binned with native 0.492 arcsec pixels. The black arrow indicates a brightness edge corresponding to the lobe edge. See text for details.

were used to define the extent of the lobe extraction regions on the X-ray data. We also used the radio fluxes within these regions to do combined modelling of the radio and X-ray spectra. No additional processing has been done to the radio data.

In the *Chandra* image, we observe a brightness edge in the eastern lobe just above the northern hotspot, that corresponds with the edge of the lobe in the VLA data. This is empirical evidence that we are directly observing the non-thermal emission from the lobe in the X-ray data in this region. We have indicated this region with a black arrow in Fig. 1.

2.2 Extraction regions and spectra

We used the `CIAO` fitting package `Sherpa` (Freeman et al. 2001) to analyse the spectra. All spectral models mentioned in this paper are multiplied by a PHABS foreground Galactic absorption model. The Galactic HI column density is set at 3.1×10^{21} atoms cm^{-2}. This value is based on the average of the column densities of the Leiden/Argentine/Bonn (LAB) and Dickey & Lockman surveys (Kalberla et al. 2005; Dickey & Lockman 1990). The thermal model used in this paper is the Astrophysical Plasma Emission Code (APEC, Smith et al. 2001), with the elemental abundance model from Anders & Grevesse (1989).

To better highlight the wealth of structure within the Cyg A cocoon shock, we created a residual map of the data. This was done by subtracting a radial unsharp masked image (Wise et al.,

in prep.). This technique is similar to traditional unsharp masking techniques. A radon transform was applied to the background-subtracted, merged image of the core. Each column of pixels was then smoothed with a 7 arcsec 1D Gaussian kernel. The smoothed image was transformed back to Cartesian coordinates and subtracted from the input image. The resulting residual map, together with the extraction regions, are shown in Fig. 2. The radial unsharp masking technique has the advantage that it only smooths in the radial direction. Therefore, there is less risk of creating artifacts by mismatched Gaussian smoothing kernels.

We assume that the X-ray jets are tube-like structures inside the lobes, which are in turn embedded in a shell of thermal ICM. With this geometry in mind, we define three different types of extraction regions: the X-ray jet regions (J), lobe regions (L) and thermal background regions (B). For each lobe, we defined 3 sets of J, L and B regions, which allows for variation in the thermal properties of the ICM along the jet axis.

The X-ray jet regions were made to trace the jet as seen on the residual map. In the eastern lobe especially, the jet makes a noticeable bend which the extraction regions follow. The width of each jet region was set to be the FWHM of the surface brightness peak perpendicular to the jet in that region. This definition results in variations in the width of the jet extraction regions along the jet path.

In defining the edges of the lobe, we have taken care to include the regions with the brightest lobe emission that lie within
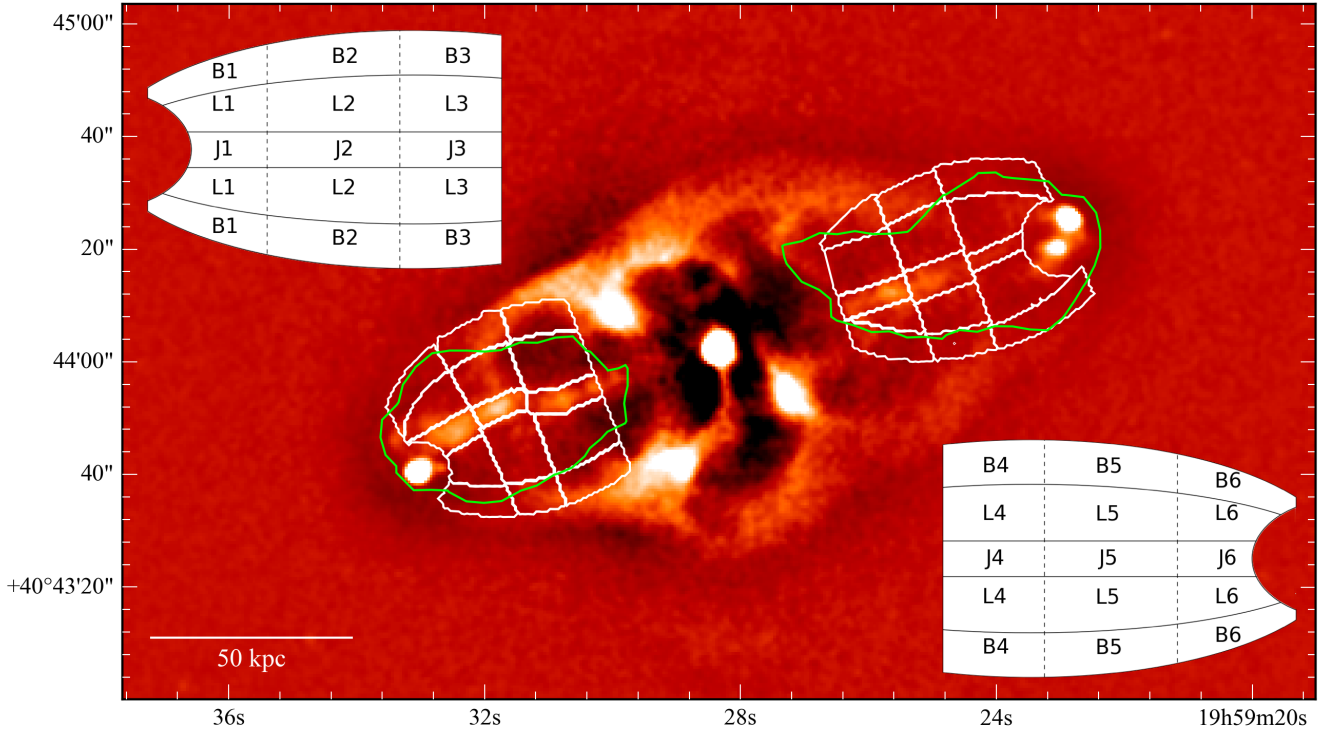
Figure 2. Radial unsharp masked residual image of the Cyg A core. Shown in green are smoothed contours of the 4.5 GHz VLA radio data. Shown in white are the jet (J), lobe (L) and background (B) extraction regions. The schematic illustrations next to each lobe indicate how the regions are labelled.

the cocoon shock. We have therefore opted to use the VLA map rather than the LOFAR map, as electrons that produce synchrotron emission at 150 MHz, will IC scatter those synchrotron photons to energies below 1 eV. Because SSC emission is considered to strongly contribute to the total IC flux, we expect regions that show only low-frequency radio emission to show less non-thermal X-ray emission.

We determined the noise level on the VLA 4.5 GHz continuum map to be 0.8 mJy/beam. We then defined contours around the lobe at the 5 σ level, or 4 mJy/beam, at a smoothing scale of 20 pixels. These contours enclose the brightest lobe emission. The lobe regions on each side were then defined as ellipses approximately following these contours. We trimmed the lobe regions close to the hotspots, as we expect the cocoon shock emission to dominate here over any possible non-thermal emission from the X-ray jet and lobes. In the western lobe, the ellipse was trimmed on the southern side to follow the asymmetric shape of the radio lobe.

Finally, the thermal background regions were created by drawing ellipses around the lobe regions on each side. These regions were defined close to the lobes so that their thermal properties do not differ much from the thermal properties of the material in front of the lobes. The outer edge of the radio lobe does enter slightly into the thermal background regions in the outer parts, although the radio lobe drops off in flux sharply beyond the defined lobe size. The thermal spectra for the background regions are not subtracted from the spectra, but rather their temperatures and abundances are used to constrain thermal emission from material superposed on the lobe and jet regions.

Using *specextract*, we extracted the events within each extraction region from every ACIS chip that overlaps with that region. We obtained source spectra, response files, and blank sky spectra

for each region on each ACIS chip of each observation. After the extraction, we combined the spectra of for all ACIS-S and ACIS-I observations with *combine_spectra*. This results in one combined spectrum, set of response files, and blank sky background spectrum for each region. We have used these combined spectra in the rest of the analysis. *combine_spectra* automatically adds all the exposure times of individual spectra together when combining. However, this means that when an extraction region falls on two different chips within the same ObsID, the exposure time of that ObsID is erroneously counted twice. We therefore re-calculated the exposure time of each spectrum manually after the combining process.

We have chosen to combine both the ACIS-I and ACIS-S spectra together into one combined spectrum for each region. This was done because the ACIS-S data only makes up 45 ks of the total 2 Ms exposure time. Furthermore, the $\sim 5 - 8$ keV temperature of the gas around Cyg A is sufficiently high that the response below 2 keV, where ACIS-S and ACIS-I are most different, is unlikely to drive the fit results. To test this, we created combined spectra for regions B2 and B4 that only include ACIS-I observations. We then compared the total combined spectra to the ACIS-I combined spectra. In both regions, the difference in temperature and abundance are less than 1%.

In the eastern lobe and jet, the combined spectra contain an average of ~ 70000 and ~ 25000 counts per region respectively. In the western lobe and jet, the combined spectra contain an average of ~ 36000 and ~ 14000 counts per region respectively. Despite the high number of counts in each region, it is difficult to disentangle thermal from non-thermal models at CCD resolution with standard fitting procedures. To illustrate this, we took the spectrum of lobe region L2 and subtracted the blank sky background for the same region. We then fit two models to this spectrum: a thermal APEC
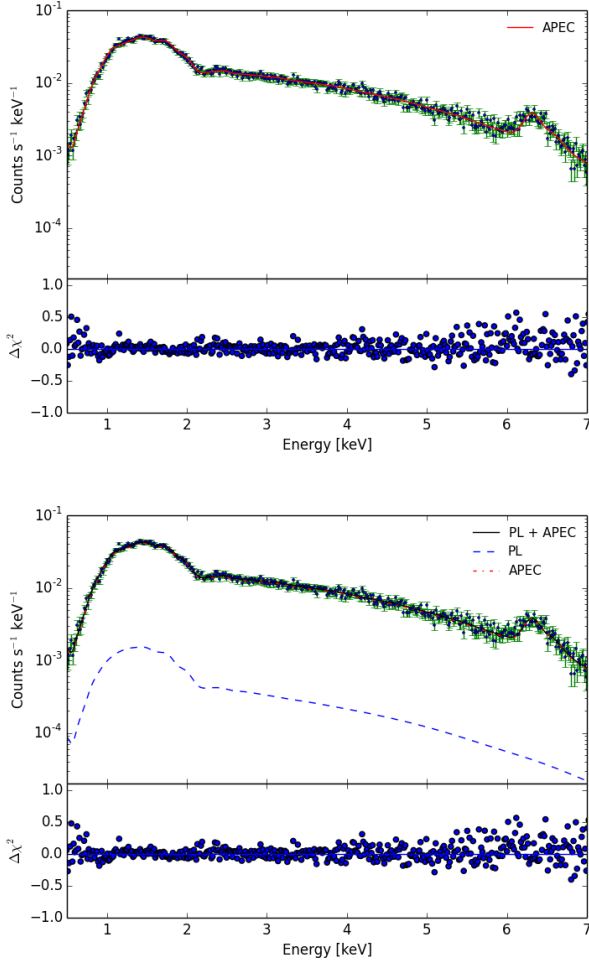
Figure 3. Comparison of two different models, both fit to the spectrum of region L2. The top image shows an `APEC` model, the bottom image a `APEC + POWERLAW` model.

model, or a combination of thermal and non-thermal emission (`APEC + POWERLAW`). The resulting fits are shown in Fig. 3. An `APEC` fit gives a χ^2/dof of 433/430, while the `APEC + POWERLAW` fit gives a χ^2/dof of 433/428.

Because the power law component is weak compared to the thermal component, the difference in the parameters between models is small: the `APEC` model gives $T = 6.36 \pm 0.09$ keV and $Z = 0.42 \pm 0.03$, while the `APEC + POWERLAW` model gives $T = 6.48 \pm 0.18$ keV and $Z = 0.44 \pm 0.03$, and $\Gamma = 2.06 \pm 0.62$. This example illustrates that when a non-thermal emission component is included in the model, the fit is not significantly improved, and that because of its small amplitude compared to the thermal component, it does not have a significant effect on the thermal parameters. Therefore, statistical tests such as an F-test do not give convincing evidence for or against the presence of power law emission.

Instead, of treating each region separately, we will treat all the regions in each jet and lobe together. By building a Bayesian model for each lobe and jet, we can simultaneously fit regions while setting priors for each of the parameters in our model. It also allows us to MCMC sample the models and thereby obtain posterior

distributions for each parameter. We describe the statistical approach and the models used in the next section.

3   STATISTICAL ANALYSIS

3.1   Statistical approach

We give a brief overview of the statistical approach here. For a more extended review of Bayesian inference, Markov Chain Monte Carlo (MCMC) sampling, and model comparison, we refer to Appendix A. The models are described in more detail in section 3.2.

We defined two competing models for the lobe regions on each side: one model with only thermal emission and one which includes both thermal and non-thermal emission. For each of these models, we determined the maximum loglikelihood through a *Maximum A Posteriori* (MAP) estimate. Each model was also sampled with a MCMC algorithm. We used the Python module *emcee* (Foreman-Mackey et al. 2013), which implements an affine invariant ensemble MCMC sampler based on Goodman & Weare (2010).

The likelihoods obtained from the MAP estimate were used to compare the models with the corrected Akaike Information Criterion (AIC_C) and the Bayesian Information Criterion (BIC). We have used the Likelihood Ratio Test (LRT) as an additional model comparison tool. The LRT is a form of hypothesis testing for the likelihood ratio between two nested models. The MCMC sampled data of the thermal model were used for the LRT, to generate fake data under the null hypothesis. We then applied a MAP for both models to this data, and compared the likelihood ratio to the likelihood ratio of the real data. With the help of these model comparison tests, we selected the most likely model and used the posterior distributions obtained from the MCMC sampling in the rest of the analysis.

We defined two competing models for the X-ray jet regions on each side as well: one thermal model and one non-thermal model. Because the jets are embedded in the lobes, the jet model needs to include all the terms from the lobe model. We used the posterior distributions from the lobe models, obtained through MCMC sampling, to set priors on the lobe components in the jet regions. As in the lobes, we determined the maximum loglikelihood of the two competing models through a MAP estimate and used AIC_C and BIC to compare the models and select the most likely model. The LRT is only valid for nested models and could therefore not be used here. The most likely model was MCMC sampled and the resulting posterior distributions were used in the rest of this analysis.

Throughout this paper, when values from the posterior distributions are quoted, we have used the median together with the 14th and 86th percentile as lower and upper errors respectively. If the data are distributed as a Gaussian, this would correspond to a 1σ credibility interval. Because the posterior distribution is not necessarily Gaussian in shape, we also show the posterior distributions that result from the MCMC sampling.

3.2   Model description

3.2.1   Source Models

The lobes and X-ray jets were analysed sequentially, so that we can apply model comparison tests first to the lobes and then to the jets. The background regions are not included in the model itself. Instead, they are fit in *Sherpa* with an `APEC` model, and the temperatures and abundances from these regions are used as priors for the thermal components in the lobe and jet models, as described in more detail

Table 2. Description of the lobe models, M_{L0} and M_{L1}, for a single lobe region.

Model component	Parameter	Prior	Hyperparameters	Description
Both models				
APEC 1	kT_1	Gaussian	$\mu = kT_1,\ \sigma = \sigma_{kT1}$	Plasma temperature
	Z_1	Gaussian	$\mu = Z_1,\ \sigma = \sigma_{Z1}$	Metal abundance
	$Tnorm_1$	half-Cauchy	$\mu = 0,\ \sigma = \sigma_{T1} \times A$	Normalisation
Hyperparameters	σ_T [a]	uniform	$10^{-7} < \sigma_T < 10^{-3}$	σ of $Tnorm_1$ half-Cauchy
M_{L1}				
POWERLAW 1	Γ_1 [a]	uniform	$1.0 < \Gamma$	Photon index
	$Pnorm_1$	half-Cauchy	$\mu = 0,\ \sigma = \sigma_L \times A$	Normalisation
Hyperparameters	σ_L [a]	uniform	$10^{-7} < \sigma_L < 10^{-3}$ [b]	σ of $Pnorm_1$ half-Cauchy

[a] These parameters are linked between regions in the same lobe. See text for details.

Table 3. Description of models M_{J0} and M_{J1}, for a single jet region.

Model component	Parameter	Prior	Hyperparameters	Description
Both models				
M_L [a]				Model M_{L0} or M_{L1}
M_{J0}				
APEC 2	kT_2 [b]	uniform	$1.0 < kT_2 < 10.0$	Plasma temperature
	Z_2 [b]	uniform	$0.0 < Z_2 < 1.0$	Metal abundance
	$Tnorm_2$	half-Cauchy	$\mu = 0,\ \sigma = \sigma_{T2} \times A$	Normalisation
Hyperparameters	σ_J [a]	uniform	$10^{-7} < \sigma_J < 10^{-3}$ [b]	σ of $Tnorm_2$ half-Cauchy
M_{J1}				
POWERLAW 2	Γ_2 [b]	uniform	$1.0 < \Gamma$	Photon index
	$Pnorm_2$	half-Cauchy	$\mu = 0,\ \sigma = \sigma_J \times A$	Normalisation
Hyperparameters	σ_J [b]	uniform	$10^{-7} < \sigma_L < 10^{-3}$ [b]	σ of $Pnorm_2$ half-Cauchy

[a] The priors for each parameter are obtained from the posterior distributions of the lobe models. The normalisation priors are scaled by the lobe/jet area ratio. See text for details.
[b] These parameters are linked between regions in the same lobe. See text for details.

in section 3.2.2. Because the definition of the edge of the lobe is somewhat arbitrary, we cannot rule out that some non-thermal emission is present in the background regions as well. However, as we have already seen in the fit comparison in section 2.2, adding a non-thermal component to the model affects the temperature and abundance very little, even in a region that is in the middle of the lobe. Therefore, the error in our assumption will likely be smaller than the width of the prior.

Each spectrum is fitted between 0.5 and 7.0 keV. In the lobe regions, we compare two different models. In model M_{L0}, every re-

gion contains a thermal model. The alternative model, M_{L1} contains the same thermal model, with a power law added to describe the non-thermal emission. The models are nested, such that $M_{L1} = M_{L0}$ when the amplitude of the power law is zero. Lobe models M_{L0} and M_{L1} are described in Table 2. We give a detailed description on the priors of the model in section 3.2.2.

Because we assume that the jets are embedded in the lobes, the jet model consists of lobe model M_L with an additional component to describe the jet. Whether the background is the thermal model M_{L0} or the model with non-thermal emission M_{L1} is determined in the model selection between M_{L0} and M_{L1}. The jet itself is modeled either as a second thermal component with the same abundance and temperature across the jet, M_{J0}, or a second power law with the same photon index across the jet, M_{J1}. The jet models M_{J0} and M_{J1} are described in Table 3. The jet models, in contrast to the lobe models, are not nested. This means that we can apply the information criteria but not the likelihood ratio test.

We note that Tables 2 and 3 show the parameters for just one set of lobe and jet regions. As indicated in the table, most parameters are different for each lobe and jet region. However, we have constrained the photon index Γ_1 and the parameters σ_L and σ_J only have one value throughout the lobe. In the jet models, we assume either a single temperature and abundance (M_{J0}), or a single photon index Γ_2 (M_{J1}) throughout the entire jet.

3.2.2 Priors

From MCMC sampling of the lobe models we obtain posterior distributions of each parameter in the model. We subsequently use these posterior distributions as priors for the jet model. The probability distributions are obtained by making a 1-dimensional Kernel Density Estimation (KDE) over the posterior distribution of each parameter. We have used an asymmetric KDE so that the smoothing effect close to the prior boundaries is minimized. This is a particular concern for some of the normalisation parameters, where most of the posterior distribution could lie close to the prior boundary at zero.

We make the assumption that any thermal or non-thermal model component in a given lobe region has the same surface brightness as that same component in the corresponding jet region. This allows us to take the posterior distributions of the thermal or non-thermal normalisation in a lobe region, scale them by area and use them as prior distributions for the jet region. Because the jet models either contain two different thermal or non-thermal model components, setting a prior on one of them makes it easier to distinguish between these two components. The assumption that the surface brightness of a component is the same in the middle of the lobe (where the X-ray jet is) as on the side, is unlikely to be completely accurate. However, assuming anything about the 3-dimensional geometry of the lobe and the jet would introduce additional uncertainties as well. Furthermore, the error in this assumption will likely be subsumed in the width of the input prior distribution.

The models use a few prior distributions which require additional parameters. Parameters of a prior distribution are referred to as *hyperparameters*. Hyperparameters can be fixed, as is the case for e.g. the peak and width of the Gaussian prior distribution on the temperature and abundance. In the case of the half-Cauchy distributions on the normalisations however, we include the hyperparameter as a free parameter in the model. The hyperprior used for those hyperparameters is a uniform prior with upper and lower bounds.

For the temperature and abundances of the foreground ICM,

we have assumed a Gaussian prior with a mean μ and a standard deviation σ. These parameters are set by performing an APEC fit to the background region adjacent to the lobe region. The results from these fit are then used to set μ and σ of the corresponding temperature and abundance prior distribution.

The normalisation parameters have a half-Cauchy prior distribution. This distribution includes the zero point, is heavy-tailed, and is recommended for scale parameters in Bayesian hierarchical models (Gelman 2006; Polson & Scott 2011). It is especially important that the normalisation prior includes zero, to satisfy the requirement of nested models.

While the peak of the half-Cauchy distribution is at zero, the σ of the distribution is a hyperparameter that is sampled in the model. We have opted to use one σ for each model component throughout all the regions, scaled by the area of that region. This was done to make each model component comparable between regions. To take σ_L as an example: if there is any non-thermal emission in the lobe regions, we would not expect there to be a lot of non-thermal emission in L1, none in L2, and a lot in L3. We therefore use one value of σ_L, scaled by area, that sets the half-Cauchy prior distributions on the non-thermal normalisations in all three regions. The three different model components each have one hyperparameter: σ_T, σ_L, σ_T. The area is indicated in Tables 2 and 3 as A.

Finally, we set a uniform prior on the photon index Γ, with a lower bound of 1. This is because we require the power law to go down with increasing energy. We note again that Γ is held constant throughout both the lobe and the X-ray jet.

We can now write out the full posterior equations for lobe models M_{L0} and M_{L1} and jet models M_{J0} and M_{J1}, for lobe spectra D_l and jet spectra D_j:

$$p(\Theta \,|\, \{D_l\}_{l=1}^{L}, M_{L0}) \propto$$

$$\left(\prod_{l=1}^{L} p(D_l \,|\, kT_1, Z_1, Tnorm_1) \, p(kT_1 \,|\, \mu_{kT}, \sigma_{kT}) \right. \qquad (1)$$

$$\left. p(Z_1 \,|\, \mu_Z, \sigma_Z) \, p(Tnorm_1 \,|\, \sigma_T \times A) \right) p(\sigma_T \,|\, min, max),$$

$$p(\Theta \,|\, \{D_l\}_{l=1}^{L}, M_{L1}) \propto$$

$$\left(\prod_{l=1}^{L} p(D_l \,|\, kT_1, Z_1, Tnorm_1, \Gamma_1, Pnorm_1) \, p(kT_1 \,|\, \mu_{kT}, \sigma_{kT}) \right.$$

$$\left. p(Z_1 \,|\, \mu_Z, \sigma_Z) \, p(Tnorm_1 \,|\, \sigma_T \times A) \, p(Pnorm_1 \,|\, \sigma_L \times A) \right) \qquad (2)$$

$$\left(p(\Gamma_1 \,|\, min, max) \, p(\sigma_T \,|\, min, max) \right),$$

$$p(\Theta \,|\, \{D_j\}_{j=1}^{J}, M_{J0}) \propto$$

$$\left(\prod_{j=1}^{J} p(D_j \,|\, M_L, kT_2, Z_2, Tnorm_2) \, p(M_L) \, p(Tnorm_2 \,|\, \sigma_{T2} \times A) \right).$$

$$\left(p(kT_2 \,|\, min, max) \, p(Z_2 \,|\, min, max) \, p(\sigma_{T2} \,|\, min, max) \right)$$

$$(3)$$

$$p(\Theta \,|\, \{D_j\}_{j=1}^{J}, M_{J1}) \propto$$

$$\left(\prod_{j=1}^{J} p(D_j \,|\, M_L, \Gamma_2, Pnorm_2) \, p(M_L) \, p(Pnorm_2 \,|\, \sigma_J \times A) \right) \quad (4)$$

$$\left(p(\Gamma_2 \,|\, min, max) \, p(\sigma_J \,|\, min, max) \right),$$

The above equations are Bayes' theorem with all likelihood and prior terms written out, for both lobe and both jet models. The first term after each product sign is the Poisson likelihood for that region. The other terms describe the prior for each of the parameters. The last terms in each equation are the priors for parameters that are linked between the regions: the photon indices Γ_1 and Γ_2, the temperature and abundance in the thermal jet model (M_{J1}), and the hyperparameters σ_T, σ_L and σ_J.

Each lobe contains 3 lobe and 3 jet regions. We analysed the eastern and western lobes individually, so per lobe we have 10 free parameters for M_{L0}, 14 free parameters for M_{L1}, 19 free parameters for M_{J0} and 18 for M_{J1}.

3.2.3 Blank sky backgrounds

Because we are using Poisson likelihoods, we cannot subtract the ACIS blank sky background spectra from the source spectra. This would make the resulting data non-Poissonian.

The ACIS blank sky backgrounds are made by averaging the backgrounds of many different ObsIDs, for each pixel on each ACIS chip. The backgrounds include both instrumental and sky components. The instrumental background can be described by a continuum and multiple fluorescent emission lines (Bartalucci et al. 2014). The sky background consists mainly of diffuse Galactic thermal emission and a weakly absorbed power law (Hickox & Markevitch 2006). Therefore, any physical model that describes the full background will have to consist of many different components. Furthermore, because of the large number of ObsIDs involved in making the backgrounds, it is not possible to create separate spectral response files for the blank sky backgrounds with the usual CIAO tools.

In our regions of interest, the contribution of the blank sky backgrounds are rather small, making up between 0.3 and 0.9% of the total counts. We have therefore opted to model the blank sky spectra for each region parametrically rather than with a physical model. For each background spectrum, we group the bins to have a minimum of 25 counts in each bin, depending on the number of counts in the background spectrum. After grouping, we interpolate a non-smoothed quadratic spline through the grouped spectrum with *scipy.interpolate.UnivariateSpline*. The spline is then scaled with the exposure time ratio between the source and background spectra.

We then take this spline to be the background model m_{BG} for that region, and we add it to the model before calculating the Poisson loglikelihood as

$$m_{\text{full}}(\Theta) = m_{\text{data}}(\Theta) + m_{BG}. \quad (5)$$

4 RESULTS

4.1 Model comparison

We first apply the AIC_C, BIC and Likelihood ratio test to the lobe regions, and select between model M_{L0} and M_{L1}. We then move on

Table 4. AIC_C and BIC model comparison for the lobe regions.

Lobe	$k_{M_{L0}}$ [a]	$k_{M_{L1}}$ [b]	n [c]	$ln(\frac{\acute{L}_1}{\acute{L}_0})$ [d]	ΔAIC_C [e]	ΔBIC [f]
East	10	14	1437	23.8	-39.6	-18.8
West	10	14	1437	18.9	-29.8	-9.0

[a] The number free parameters in M_{L0}.
[b] The number of free parameters in M_{L1}.
[c] The total number of data points (i.e. spectral channels).
[d] The log-likelihood ratio of the best-fit likelihoods to M_{L0} and M_{L1}.
[e] The difference in the AIC_C between M_{L0} and M_{L1}. Positive values indicate evidence in favour of M_{L0}, negative values indicate evidence in favour of M_{L1}.
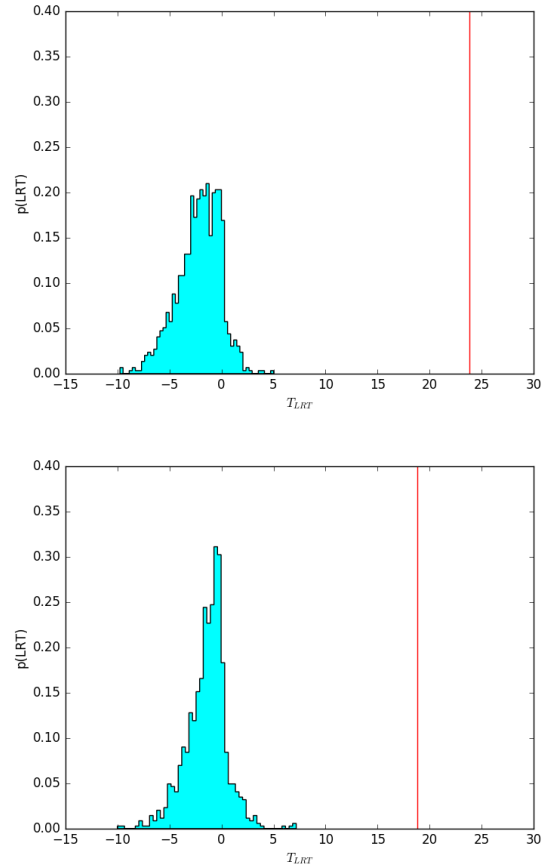[f] As above, for the BIC.

Figure 4. Top: Likelihood-ratio distribution for M_{L0} and M_{L1} in the eastern lobe. The likelihood ratio of the real data is shown as a red line. Bottom: As above, for the western lobe.

to the jet regions, where we use either M_{L0} and M_{L1} as part of the jet model and select between M_{J0} and M_{J1}.

4.1.1 The lobes

In the lobes, we compared a model with a single thermal component, M_{L0}, with a model containing both a thermal and non-thermal component ,M_{L1}. The AIC_C and BIC values are shown in Table 4. We refer to Table A1 for the relation between AIC_C or BIC and the

Table 5. AIC_C and BIC model comparison for the jet regions.

Lobe	k_{M_0} [a]	k_{M_1} [b]	n [c]	$ln(\frac{\hat{L}_1}{\hat{L}_0})$ [d]	ΔAIC_C [e]	ΔBIC [f]
East	19	18	1437	-1.0	-0.2	-5.5
West	19	18	1437	1.5	-5.0	-10.3

[a] The number free parameters in M_{J0}.

[b] The number of free parameters in M_{J1}.

[c] The total number of data points (i.e. spectral channels).

[d] The log-likelihood ratio of the best-fit likelihoods to M_{J0} and M_{J1}.

[e] The difference in the AIC_C between M_{J0} and M_{J1}. Positive values indicate evidence in favour of M_{J0}, negative values indicate evidence in favour of M_{J1}.

[f] As above, for the BIC.

strength of the evidence for or against a given model. Both information criteria show a strong preference for model M_{L1}. It should be noted that the number of data points n may be overestimated, as the number of spectral bins is higher than the spectral resolution. Thus, adjacent spectral bins are strongly correlated and the number of spectral bins is not an accurate representation of the sample size n. To get around this problem, the concept of an 'effective sample size' is used in some fields (e.g. Thiébaux & Zwiers 1984). However, lowering the sample size will skew the results even more towards model M_{L1}, and it will therefore not influence our conclusion of M_{L1} as the most likely model.

The results of the likelihood ratio test are shown in Fig. 4. For each lobe, we calculated the likelihood ratio 1000 times. We find that none of the simulated likelihood ratios come close to the real likelihood ratio, which means that the p-value in both lobes is significantly smaller than 0.001. Together with the information criteria, we have strong evidence in favour of model M_{L1}. This confirms the presence of non-thermal X-ray emission in the lobes at high significance. M_{L1} will be used as part of the jet model in all subsequent analysis.

4.1.2 The X-ray jets

The model comparison tests in the lobe regions strongly prefer model M_{L1} over M_{L0}. Therefore, in the jet regions, we compared two different models with 3 components, of which the first two components are the thermal and non-thermal components of M_{L1}. We added either a thermal component, M_{J0}, or a non-thermal component, M_{J1}, to model the jet emission. The results of the model comparison between M_{J0} and M_{J1}, with AIC_C and BIC, are listed in Table 5.

In the eastern jet, the likelihood ratio $ln(\frac{\hat{L}_1}{\hat{L}_0})$ is negative, meaning that the thermal model M_{J0} has a higher likelihood than the non-thermal model M_{J1}. However, because M_{J0} has more parameters, BIC prefers model M_{J1} and AIC_C is close enough to zero as to be inconclusive. In the western jet, both information criteria show clear preference for model M_{J1}. We note that, as in the model selection of the lobes, the number of spectral channels n might not be a correct representation of the amount of independent data points because the width of each channel is smaller than the spectral resolution of ACIS. Lowering n would bring the AIC_C and BIC values closer to each other, skewing the AIC_C further towards M_{J1} and the BIC towards M_{J0}. For example, setting $n = 300$, will yield $\Delta AIC = -1.2$ and $\Delta BIC = -3.9$ in the eastern jet and $\Delta AIC = -6.0$ and ΔBIC
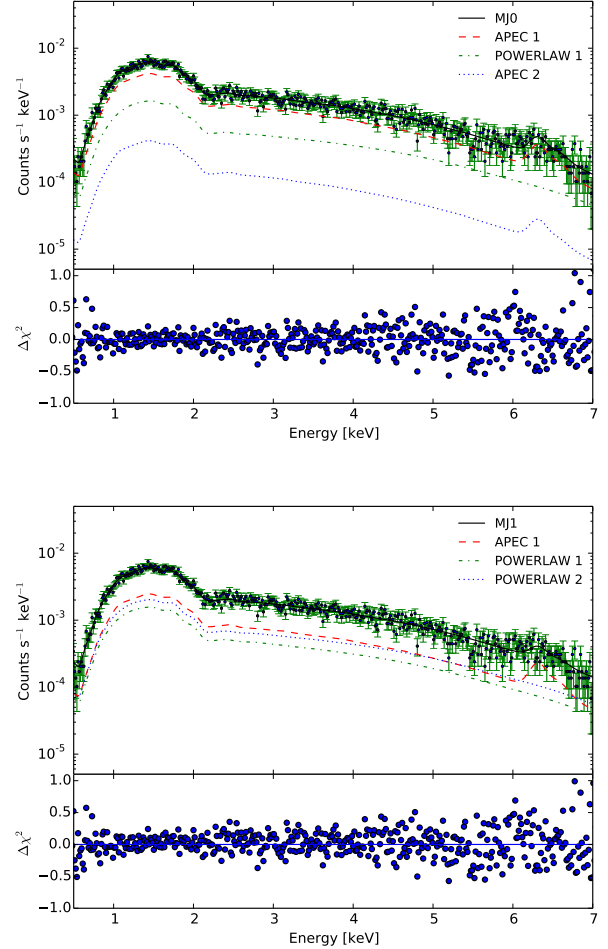
Figure 5. Comparison of models M_{J0} (top) and M_{J1} (bottom) in region J1.

$= -8.7$ in the western jet, indicating moderate to strong evidence for M_{J1}.

In the eastern jet, at the maximum posterior of model M_{J0}, we find that a thermal X-ray jet would have $T = 5.7$ keV and $Z = 0.21$ $Z_\odot$. However, the spectral normalisation of the jet component is lower than what would be expected based on the surface brightness. For example, the spectral normalisation of the jet in region J1 is about 10 times lower than that of the ICM thermal component. In the western jet, a thermal jet would have $T = 8.0$ keV and $Z = 0.10$ $Z_\odot$, but the spectral normalisation is multiple orders of magnitude below the ICM thermal component, or effectively zero.

Fig. 5 shows a comparison of models M_{J0} and M_{J1} in jet region J1, illustrating that the jet component has much lower normalisation in M_{J0}. In both the eastern and the western side, the emission from the jet is mostly attributed to the ICM thermal emission. Optimizing the posterior does not produce reasonable parameters for a thermal jet model. Combined with the results from the AIC_C and BIC, which all point in favour of model M_{J1}, we conclude that the favoured model includes a non-thermal emission component to describe the jet emission. In the analysis that follows, we will therefore use model M_{L1} in the lobe regions and M_{J1} in the jet regions.

Table 6. The thermal properties of the background, lobe and jet regions. Background regions were fit with a `PHABS x APEC` model. The temperatures and abundances are shown with 1σ errors. The temperatures and abundance posterior distributions of the lobe and jet regions are taken from models M_{L1} and M_{J1}.

Region	kT (keV)	Z ($Z_\odot$)	χ^2/dof
B1	6.80 ± 0.30	0.41 ± 0.05	$524.12 / 521$
L1	$6.54^{+0.16}_{-0.16}$	$0.47^{+0.05}_{-0.05}$	
J1	$6.53^{+0.17}_{-0.17}$	$0.46^{+0.05}_{-0.05}$	
B2	6.30 ± 0.11	0.61 ± 0.04	$684.04 / 625$
L2	$6.35^{+0.10}_{-0.10}$	$0.55^{+0.04}_{-0.04}$	
J2	$6.36^{+0.11}_{-0.11}$	$0.55^{+0.04}_{-0.04}$	
B3	5.48 ± 0.12	0.68 ± 0.04	$867.23 / 812$
L3	$5.77^{+0.08}_{-0.08}$	$0.72^{+0.03}_{-0.03}$	
J3	$5.79^{+0.09}_{-0.09}$	$0.71^{+0.03}_{-0.03}$	
B4	5.91 ± 0.13	0.52 ± 0.04	$805.63 / 774$
L4	$5.97^{+0.20}_{-0.20}$	$0.60^{+0.06}_{-0.06}$	
J4	$6.06^{+0.20}_{-0.21}$	$0.58^{+0.05}_{-0.05}$	
B5	6.80 ± 0.20	0.49 ± 0.05	$720.10 / 696$
L5	$7.19^{+0.38}_{-0.32}$	$0.53^{+0.07}_{-0.06}$	
J5	$7.02^{+0.34}_{-0.25}$	$0.59^{+0.07}_{-0.06}$	
B6	7.72 ± 0.26	0.38 ± 0.05	$707.86 / 711$
L6	$8.03^{+0.46}_{-0.43}$	$0.41^{+0.08}_{-0.07}$	
J6	$8.00^{+0.46}_{-0.43}$	$0.42^{+0.08}_{-0.07}$	

4.2 Thermal emission components

The results for the thermal properties of the background, lobe and jet regions are listed in Table 6. As described in section 3.2, the temperatures and abundances of the background regions were obtained by fitting a `PHABS X APEC` model to the spectra with *Sherpa*. The obtained values were then used as priors for the lobe model, and the distributions from the lobe models were in turn used as priors for the jet model. Table 6 shows that none of the temperatures and abundances within a set of background, lobe and jet regions deviate significantly from each other.

Consistent with Snios et al. (2018) and Wise et al. (in prep), we observe that the temperatures increase with distance from the AGN and significantly higher temperatures on the western side than on the east Our results are also broadly consistent with the temperatures found by Wilson et al. (2006) in the regions around the lobe.

The inner background regions B3 and B4 are just on the edge of the bright, rib-like structures extending outward from the AGN. Duffy et al. (2018) suggest that these rib-like structures are a result of the destruction of the cool core during initial passage of the radio jet. Thermal plasma from the cool core would then be pushed into a cylindrical rib-like shape by backflow antiparallel to the direction of the jet. The ribs have temperatures of around 2.5 - 4.5 keV (Chon et al. 2012; Duffy et al. 2018), making them significantly cooler than the background regions. The background regions defined in this work have a significantly higher temperature and thus can be assumed to be part of the cocoon shock, rather than the rib-like structures. Table 6 does show a slightly worse fit quality regions B3 and B4, which could indicate some mixing with enriched gas from the core. However, the reduced χ^2 values in these regions, 1.07 for B3 1.03 for B4, show that these are still acceptable fits.

Table 7. Flux density and power law of the non-thermal emission from the jets and lobes.

		S_{1keV} [a] (nJy)	Γ
East	Lobe	71^{+10}_{-10}	$1.72^{+0.03}_{-0.03}$
	Jet	24^{+4}_{-4}	$1.64^{+0.04}_{-0.04}$
West	Lobe	50^{+12}_{-13}	$1.97^{+0.23}_{-0.10}$
	Jet	13^{+4}_{-5}	$1.86^{+0.18}_{-0.12}$

[a] Flux density at 1 keV

4.3 Non-thermal emission components

From the model comparison we conclude that there is non-thermal emission from both the lobes and the X-ray jets. This means that in each set of lobe and jet regions, there are 3 non-thermal components and 3 associated normalisations: $Pnorm_{1,L}$ for the normalisation of the lobe emission in the lobe region, $Pnorm_{1,J}$ for the normalisation of the lobe emission in the jet region, and $Pnorm_{2,J}$ for the normalisation of the jet emission. Correspondingly, there are also 3 photon indices: $\Gamma_{1,L}$ for the lobe emission in the lobe regions, $\Gamma_{1,J}$ for the lobe emission in the jet regions, and $\Gamma_{2,J}$ for the jet emission. Because we used the posterior distributions from the lobe regions as a prior to constrain the lobe emission in the jet region, we expect these posterior distributions to look similar. We comment further on this in section 5.1.

We show the posterior distributions of the non-thermal emission components from the lobes and jets in Figs. 6 and 7. We list the total flux and the photon index of each lobe and each jet in Table 7. We note that the lobe flux densities on the eastern and western side are consistent with those found by Yaji et al. (2010) and Hardcastle & Croston (2010). For plots showing the correlation between the normalisation and photon index of each component in each region, we refer to Appendix B.

We compared the photon indices obtained from the posterior distributions to the radio spectral index. Spinrad et al. (1985) finds an average low-frequency spectral index α of 0.74 for the lobes. This agrees well with our photon index of $1.72^{+0.03}_{-0.03}$ in the eastern lobe, but not with the value of $1.97^{+0.23}_{-0.10}$ in the western lobe. We discuss possible causes for the differences between the lobes in section 5.3.

4.4 Non-thermal pressure in the lobes and X-ray jets

4.4.1 The lobes

The parameters for the non-thermal emission that we find under model M_{L1} and M_{J1} were used to model the pressure in the lobes. We compared the pressures found from the models with the rim pressures as calculated by Snios et al. (2018). These pressures are determined from X-ray spectra of compressed gas in regions between the cocoon shock and the lobes. The average rim pressures for the eastern and western lobe are $p_{rim,east} = (10.4 \pm 0.4) \times 10^{-10}$ erg cm^{-3} and $p_{rim,west} = (8.4 \pm 0.2) \times 10^{-10}$ erg cm^{-3}. By comparing the rim pressures with the non-thermal pressures from our models we are able to constrain lobe parameters such as the fraction of non-radiating particles and the lower limit to the electron energy distribution, denoted as κ and γ_{min} respectively.

The IC pressures were modeled with the inverse-Compton code of Hardcastle et al. (1998), called *synch*. The code takes into account both IC/CMB as well as SSC, which is an important component in
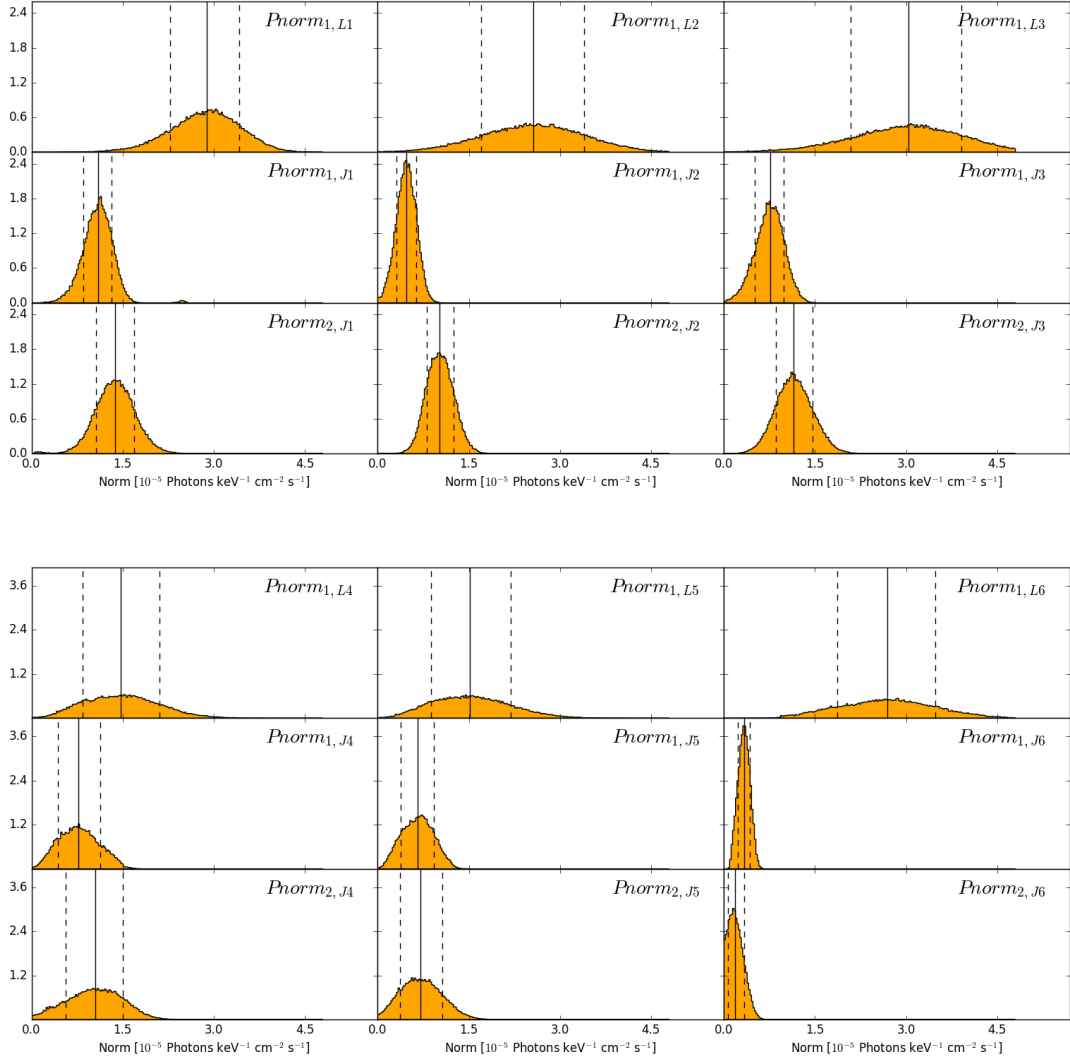
Figure 6. Top: Posterior distributions for the power law normalisations in the eastern lobe. Normalisations indicate the photon flux density at 1 keV. The top row shows the non-thermal emission in each lobe region. The middle row shows the non-thermal lobe emission in each jet region, and the bottom row shows the non-thermal jet emission each jet region. The solid lines indicate the median, the dashed lines the 14th and 86th percentiles. Bottom: As above, for the western lobe.

Table 8. Comparison of the rim lobe pressures to the modeled IC lobe pressures, for $\kappa = 0$.

	p_{rim} [a] $(10^{-10}\,\text{erg cm}^{-3})$	γ_{min} [b]	p_{IC} [c] $(10^{-10}\,\text{erg cm}^{-3})$	B (μG) [d]
East	10.4 ± 0.4	1	$5.8^{+2.0}_{-1.4}$	42^{+3}_{-3}
		10	$2.2^{+0.4}_{-0.4}$	42^{+3}_{-3}
West	8.4 ± 0.2	1	140^{+1690}_{-116}	45^{+15}_{-5}
		10	18^{+40}_{-10}	45^{+15}_{-5}

[a] The rim pressures for the eastern and western lobe, taken from Snios et al. (2018).
[b] The lower cutoff to the electron energy distribution.
[c] The IC pressures, obtained from *synch*. See text for details.
[d] The magnetic field strength, obtained from *synch*.

Table 9. The IC relic jet pressures, for $\kappa = 0$.

	γ_{min} [a]	p_{IC} [b] $(10^{-10}\,\text{erg cm}^{-3})$	B (μG) [c]
East	1	$7.9^{+5.8}_{-3.3}$	27^{+5}_{-4}
	10	$4.0^{+2.6}_{-1.3}$	27^{+5}_{-4}
West	1	99^{+540}_{-76}	17^{+7}_{-3}
	10	22^{+40}_{-12}	17^{+7}_{-3}

[a] The lower cutoff to the electron energy distribution.
[b] The IC pressures, obtained from *synch*. See text for details.
[c] The magnetic field strength, obtained from *synch*.

the Cyg A lobes (Hardcastle & Croston 2010; Yaji et al. 2010). The code calculates the total energy density in a certain volume,
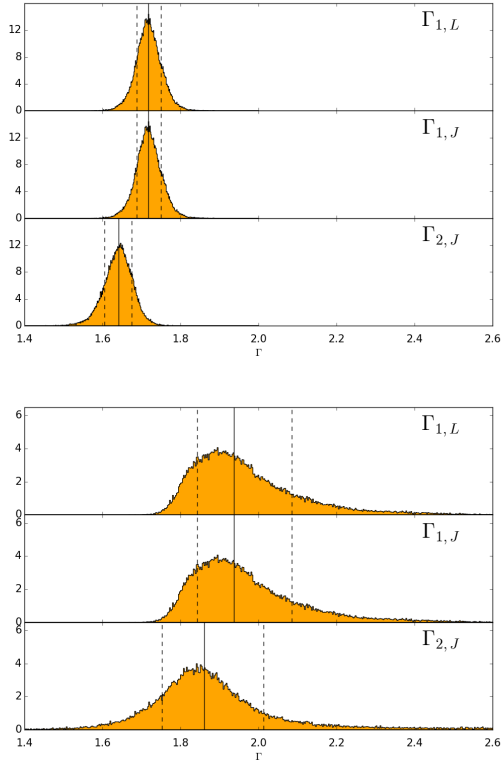
Figure 7. Top: Posterior distributions for the power law photon indices in the eastern lobe. The top figure shows the photon index of the non-thermal emission in the lobe regions. The middle figure shows the photon index of the non-thermal lobe emission in the jet regions. The bottom figure shows the photon index of the non-thermal jet emission in the jet regions. The solid lines indicate the median, the dashed lines the 14th and 86th percentiles. Bottom: As above, for the western lobe

including the energy density from both particles and the magnetic field. We have modeled the electron distributions as broken power laws with an age break.

We calculated the volume of each lobe by approximating them as a capped ellipsoid, inclined to the line of sight with an angle of 55 degrees (Vestergaard & Barthel 1993), based on the lobe region sizes. We obtain total volumes of 6.8×10^{68} cm^3 for the eastern lobe, and 7.4×10^{68} cm^3 for the western lobe.

We normalised the synchrotron spectrum to the flux inside the lobe and jet regions on the 4.5 GHz VLA radio map (Carilli et al. 1991). Because no radio brightness enhancement is observed at the location of the X-ray jet, we assume that all of the radio emission in the lobe and jet regions can be attributed to the lobes. We find flux densities 211 Jy for the eastern lobe and 156 Jy for the western lobe.

The break frequency ν_B varies over a range from 1 to 10 GHz in the lobes of Cyg A (Carilli et al. 1991). We have modeled each lobe with a single average break frequency of 5GHz. We have assumed that the photon index increases by 0.5 beyond the break frequency. Initial runs with *synch* show that the magnetic field in the lobes is around ∼ 40 μG. This translates to electron Lorentz factors of $\gamma_B \sim 7000$ at the break frequency.

The choice for the lower cutoff to the electron energy distribution, γ_{min}, can significantly affect the calculated pressure. The higher the photon index, the steeper the slope, and the more the low-

energy electrons contribute to the total pressure. The value of γ_{min} is unknown, we calculate the pressures for $\gamma_{min} = 1$ and $\gamma_{min} = 10$. The upper cutoff to the electron distribution was set at $\gamma_{max} = 10^5$, giving a cutoff in the synchrotron spectrum at $\simeq 10^{12}$ Hz.

The slope of the electron energy distribution, p, is directly related to the photon index by $p = 2\Gamma - 1$. We have used Γ from our models to determine p. We now have assumptions for γ_{min} and γ_{max}, the photon indices and normalisations of the IC spectrum as determined from the posterior distributions, and the normalisation and ν_B of the synchrotron spectrum determined from the VLA radio data. With these, the magnetic field strength and energy density in the lobe can be modeled with *synch*.

We initially assumed an equipartition magnetic field and determined what the predicted X-ray flux would be in this case, using the median value of the photon index posterior distribution. Assuming $\gamma_{min} = 1$, we find equipartition fields of 95 μG and 210 μG in the eastern and western lobe respectively. For $\gamma_{min} = 10$, the equipartition fields are 73 μG and 130 μG. However, for both values of γ_{min} the equipartition field underpredicts the observed X-ray flux by factors of a few, implying that the true magnetic field is below the equipartition value.

We then modeled the lobe pressure and magnetic field strength by using the observed X-ray flux from the posterior distributions. For each lobe, we took 300 random samples of the non-thermal normalisation and photon index, and ran *synch* for each of these parameter sets. The resulting distributions of the model pressure for each lobe, and a comparison with the rim pressures, are shown in Table 8.

In the calculations above we have assuming that the fraction of non-radiating particles in the lobe, κ, is zero. Because the magnetic field strength is below equipartition, the total energy is dominated by the particle energy. We can thus assume the IC pressures to scale linearly with $\kappa + 1$.

As was previously reported by Hardcastle & Croston (2010), we find that the non-thermal lobe flux in both lobes is dominated by SSC. In the eastern lobe, SSC makes up about 80% of the total non-thermal flux. In the western lobe, the ratio spread is wider because of the wider distribution of Γ, but SSC makes up about 50-90% of the non-thermal flux.

4.4.2 The X-ray jets

We have modeled the X-ray jets as an inverse-Compton emitting population of electrons, with *synch*. This corresponds to the IC relic jet model proposed by Steenbrugge et al. (2008). The energy density and pressure in the X-ray jet can be calculated in the same manner as the lobes and compared to the lobe and rim pressures on each side.

For the volume, we have used the defined jet regions and assumed that they are tubular in shape. We also assume an inclination angle to the line of sight of 55 degrees. This yields total volumes of 3.8×10^{67} cm^3 and 4.2×10^{67} cm^3 for the eastern and western jets respectively.

It is difficult to model the synchrotron spectrum from the X-ray jets, because little to no emission is observed from these features. In the IC relic jet model, the adiabatic expansion of the jet should cause the Lorentz factors of the electron population to go down. The adiabatic expansion combined with synchrotron aging caused the relic to have faded beyond detection at radio wavelengths.

We have looked for evidence of the relic jet in the LOFAR 150 MHz data (McKean et al. 2016). In the eastern lobe, we observe an enhancement in the brightness and spectral index map at roughly

the location of the relic jet. However, the enhancement seems to be between two of the X-ray jet knots. In the western lobe, there is a slight brightness enhancement as well, although the corresponding spectral index enhancement is weaker than in the eastern lobe. Similarly, the enhancement is on the path of the relic jet, but not at the same location as the X-ray jet knot. In both lobes, there seems to be a faint brightness enhancement that is roughly aligned with the path of the relic jet. These brightness and spectral index enhancements, although weak and not well aligned, provide a hint that the X-ray jets are non-thermal in origin, consistent with our results from the model comparison.

Regardless of whether the radio features seen in the LOFAR maps are associated with the X-ray jet, it is difficult to determine what the radio spectrum of the IC relic jet would look like. We have used the LOFAR radio map to set an upper limit to the number density of electrons in the relic jet plasma. At most, the radio emission per unit volume of the relic jet on the 150 MHz LOFAR map cannot be more than that of the lobe. Using this assumption, we obtain maximum flux densities of 220 Jy at 150 MHz for the eastern jet, and 155 Jy at 150 MHz for the western jet. We note that this upper limit to the radio flux effectively corresponds to a lower limit on the modeled pressures. The lower the radio flux, the further below equipartition the relic jet will be, and the higher the modeled IC pressure.

While the relic jet only generates a relatively small number of synchrotron photons, it is embedded inside the lobe and subjected to its synchrotron photon field. We therefore also considered a third IC component, which is the external Compton of the lobe and hotspot photon fields passing through the jet. We modeled the spectrum of the lobe by assuming that the radio emission mechanism is isotropic, and we assumed that the emission coefficient j_ν, is a constant throughout the lobe. The average intensity at a specific wavelength is then

$$J_\nu = j_\nu \int \frac{dV}{4\pi \ell^2}, \qquad (6)$$

where V indicates the volume, ℓ the path along a ray from the source to the region of interest, and J_ν the average intensity. We assume axial symmetry for the lobe, and use cylindrical polar coordinates r, ϕ, z. Then, integrating over the angle ϕ yields

$$J_\nu = j_\nu \int \frac{r \, dr \, dz}{2\sqrt{\{z^2 + (r - x_0)^2\}\{z^2 + (r + x_0)^2\}}}, \qquad (7)$$

where x_0 is the distance from the axis of the point of interest in the plane $z = 0$. We evaluate the intensity at the centre of the jet ($x_0 = 0$). We also assume the jet is a cylindrical tube inside the lobe, and so we integrate over the cylinder radius r between $r_j(z)$ and $r_l(z)$. This reduces the integral to a 1-dimensional integral over z:

$$J_\nu = \frac{j_\nu}{4} \int \ln\left(\frac{z^2 + r_l^2}{z^2 + r_j^2}\right) dz. \qquad (8)$$

The radius of the lobe and the jet, r_j and r_l, are both functions of z. We have approximated both functions for each lobe by manually measuring the radius at several points along the z-axis and linearly interpolating between these points.

We used equation 8 along with the radio flux from the VLA data, to calculate the average intensity at 4.5 GHz. We then modeled the spectrum of the lobe as a broken power law, using a break frequency of 5GHz. The spectral index of the lobe model is drawn directly from the posterior distributions and therefore varies from sample to sample.

Additionally, we estimated the influence from the hotspots by modelling them as point sources. We again took the radio flux of the hotspots from the VLA data, finding flux densities of 117 Jy for the eastern hotspots and 152 Jy for the western hotspots. We then calculated the average flux between the minimum and maximum hotspot - jet distance. We modeled the hotspot spectrum as a broken power law, with a break frequency at 10GHz and a photon index of 1.5.

Because the spectrum of the relic jet is unknown, an assumption for the break frequency has to be made. If the break frequency in the radio spectrum is too low, the IC spectrum would have a turnover below the 0.5 - 7.0 keV range, and the photon index that we see in the X-ray data would be the photon index beyond the turnover. We consider this unlikely, especially in the eastern X-ray jet, as the slope before the turnover would then be as flat as ~ 1.1. This places constraints on how low the break frequency can be. By modelling the jets with *synch*, we find that the break frequency should not be lower than ~ 4 GHz. Below that value, Compton scattering of synchrotron photons originating from the lobes, the dominant component in the X-ray jet flux, starts to turn over enough that it noticeably affects the slope of the total IC spectrum. We therefore place the break frequency at this value. The break frequency of 4 GHz and a magnetic field strength of 30 μG correspond to an electron break Lorentz factor $\gamma_B \sim 7000$. The same cutoffs and lower and upper limits were applied as for the lobes: the minimum frequency for the synchrotron spectrum is 1 MHz. The jet pressures were calculated for $\gamma_{min} = 1$ and $\gamma_{min} = 10$. The maximum electron Lorentz factor was set at $\gamma_{max} = 10^5$, which gives a cutoff in the synchrotron spectrum at $\sim 10^{13}$ Hz.

We calculated the distribution of model pressures the same way as for the lobes: we took 300 random samples from the posterior distributions of the jet normalisation and photon index. We assumed $\kappa = 0$ and we calculate pressures for both $\gamma_{min} = 1$ and $\gamma_{min} = 10$. The results are listed in Table 9. We find that external Compton scattering dominates the total flux. In the eastern jet, we find that the external Compton from the lobe photons contributes approximately 65% to the total flux, SSC of the jet photons approximately 15%, and IC/CMB scattering 20%. In the western jet, the wider distribution of Γ causes a greater spread in these fractions. External Compton of the lobe photons contributes $40 - 60\%$, SSC of the jet photons $5 - 30\%$ and IC/CMB scattering $5 - 40\%$. This seems shows that the relic jet is not purely an IC/CMB X-ray source, but that SSC needs to be taken into account in an IC relic jet model.

5   DISCUSSION

5.1   Disentangling the lobe and jet emission components

The fact that the model in the jet regions contains two separate power laws with similar photon indices, means that degeneracies are a concern. It is possible that the MCMC routine in the jet regions does not manage to fully disentangle the lobe emission from the jet emission. We have attempted to minimise this problem by making the amount of lobe emission in the lobe regions a prior for the amount of lobe emission in the jet regions. By assuming that the surface brightness of the non-thermal lobe emission is constant, the MCMC routine has less difficulty separating the non-thermal emission in the jets into two different components.

From the middle and bottom rows of both panels of Fig. 6, it appears that the two power laws can be distinguished from one another in every region. If they were not, we would expect to see

most of the non-thermal emission attributed to just one of the power laws and the other posterior distribution approaching zero. Instead, the results show distinct unimodal peaks for the lobe component and the jet component in each jet region.

Because we used the posterior distributions of $Pnorm_{1,L}$ and $\Gamma_{1,L}$ from the lobe model as priors for the parameters $Pnorm_{1,J}$ and $\Gamma_{1,J}$ in the jet model, we expect the posterior distributions of the corresponding jet and lobe parameters to be very similar. We compared the prior distributions to test this, and find that the median and the spread of each distribution agrees to a few % precision. This indicates that the MCMC routine for the jet regions did not stray far from the prior distributions given by the MCMC sampling of the lobe regions. Our assumption of constant surface brightness between a lobe region and its corresponding jet region seems therefore to be reasonable.

We investigated whether the ratio of jet to lobe flux on each side, obtained from the posterior distributions, agrees with the jet to lobe count ratio from the event data. The count ratio is determined from the event files as follows: we determine the number of counts in the jet region. We then subtract the number of counts in the lobe region, scaled to the area of the jet region. We then assume that 50-70% of the counts in the lobe region are thermal, and subtract this number from both the lobe and the jet. We are then left with estimates for the number of non-thermal counts in the lobe and the jet. In the eastern lobe, we find a flux ratio of $1.5^{+0.6}_{-0.4}$, and a count ratio of $2.0 - 2.7$. On the western side, we find a flux ratio of $1.1^{+0.9}_{-0.6}$ and a count ratio of $1.7 - 2.1$.

The count ratio is slightly higher than the flux ratio on both sides, which raises the possibility that our model underestimates the jet flux. However, the higher count ratio translates to only a modest difference in the jet flux. In the eastern jet, a count ratio of $2.0 - 2.7$ corresponds to a jet flux of 26 - 28 nJy, while in the western jet a count ratio of $1.7 - 2.1$ corresponds to a jet flux of 15 - 17 nJy. Both estimates are within the errors of the jet flux distribution from the model. The estimate provided by the count ratio seems to agree well with the flux ratio obtained from the model.

5.2 A two-temperature thermal model for the ICM

As shown in section 4.2, there is a significant difference between the ICM on the eastern and the western side of Cyg A. The temperature increase on the western side is in the direction of the merger with nearby subcluster Cyg NW, and roughly corresponding to the direction of the outburst. The fact that the temperature increase is only on one side would suggest that a shock created by the merger is the underlying cause of the temperature increase. Moreover, it is possible that the merger shock has enhanced features that were already there, perhaps imprints of previous cycles of AGN activity, or features created by sloshing motions. For a more extended discussion of the complex merger region, we refer to Wise et al. (in prep.).

Regardless of the cause of the temperature difference between east and west, there is reasonable cause to suspect that the ICM surrounding the western cocoon shock may actually be better described by a two-temperature thermal plasma. For example, one could imagine a geometry where the ICM shocked by the merger is a layer of hot ∼ 10 keV material that is partly projected in front of the lobe, while the underlying ICM has a temperature of ∼ 6 keV, the same as on the eastern side.

Mazzotta et al. (2004) have investigated the effect of fitting a single-temperature thermal model to a two-temperature plasma with

Chandra. For high gas temperatures (> 5 keV, and low abundances (< 1.0 Z$_\odot$), they find that a single-temperature thermal model fit is often statistically indistinguishable from a fit with a two-temperature thermal model. This is because when the gas temperature is high, the gas will be more highly ionised, making it more difficult to distinguish spectra with differing temperatures. In the case of Cyg A's western lobe, assuming two temperature components of ∼ 6 and ∼ 10 keV, and an abundance of ∼ 0.5 Z$_\odot$, the results from Mazzotta et al. (2004) indicate that the emission from this plasma would be very well fit by a single-temperature thermal model. Although the structure of the hot plasma around the western lobe might be complex, we therefore expect that using a single-temperature thermal model provides an adequate enough description of the spectral data.

5.3 Difference between the eastern and western lobes

The posterior distributions show clear differences between the eastern and western side, with the western side being both fainter and having a steeper X-ray spectrum. The steeper X-ray spectrum maps onto a steeper electron spectrum with a larger fraction of electron energies with low γ. This translates into higher energy densities and pressures on the western side.

The photon index on the eastern side agrees well with the value of Spinrad et al. (1985), as well as with the spectral index obtained from the LOFAR data by McKean et al. (2016). All of these show average spectral indices $\alpha \sim 0.7$.

If the photon index in the western lobe accurately reflects the average photon index, we suggest that either aging or adiabatic losses may have caused a turnover in the IC spectrum somewhere below 7.0 keV. This would explain why the photon index is higher and less constrained. It would also mean the pressures calculated by *synch* are overestimated on the western side, because the low γ range of the electron energy spectrum would have a lower photon index than we have modeled.

We looked at the available VLA and LOFAR data to see if there are differences between the lobes in the radio. In both radio maps, we find that the western lobe is roughly 30% fainter than the eastern lobe. However, there appear to be no appreciable differences between the lobes in terms of spectral index and break frequency (Perley et al. 1984; McKean et al. 2016).

Snios et al. (2018) estimate that the total volume of the western lobe is about 40% larger than the eastern lobe. Their estimate includes the volume of the shocked cocoon not just of the lobes. We note that in our own estimate of the lobe volume, the western lobe is only about 10% larger than the eastern lobe. However, the lobe regions that we have defined do not exactly follow the radio lobe, and also have the hotspot regions cut out. Therefore, the volume calculated from the lobe regions is not necessarily accurate for the lobe as a whole.

If the western lobe is indeed bigger than the eastern lobe by a few tens of percent, then this could indicate additional adiabatic expansion on the western side, which would reduce both the magnetic field strength and the particle energies. Under simple assumptions for adiabatic expansion, $B \propto V^{-2/3}$ and $\gamma \propto V^{-1/3}$, which means we would expect the magnetic field strength in the western lobe to be 80% of that in the eastern lobe. The magnetic field strengths in Table 8 do not differ significantly between east and west, although the errors on the western side are large.

For a synchrotron spectrum, the Lorentz factor of an emitting

electron and the emitted frequency are related as

$$\nu \simeq \frac{\gamma^2 q B}{2\pi m_e}, \tag{9}$$

while in the corresponding SSC spectrum, the Lorentz factor is related to the energy as

$$E = \frac{\gamma^4 \hbar q B}{m_e} . \tag{10}$$

Equation 10 and the scaling relations for B and γ imply that the characteristic energy scales with the volume as $E \propto V^{-2}$. If the western lobe is 40% bigger, the turnover in the IC spectrum of the western lobe could therefore be at 50% of the energy of that of the eastern lobe.

A break frequency ν_B at 5 GHz and a magnetic field strength of around 40 μG, yield break Lorentz factor $\gamma_B \sim 7000$, and a break energy $E_B \sim 1$ keV. This means that a turnover of the SSC part of the spectrum would be a plausible explanation for the steeper spectrum in the western lobe, especially because SSC makes up a significant amount of the total non-thermal flux in the lobes. To look for evidence of a spectral turnover, we re-evaluated the lobe spectra in two separate energy bands of 0.5 - 2.0 keV and 2.0 - 7.0 keV. We repeated the MCMC analysis of model M_{L1} in both lobes, allowing each energy band to have a different photon index. In the eastern lobe, we find $\Gamma_{0.5-2.0} = 1.56^{+0.07}_{-0.07}$ and $\Gamma_{2.0-7.0} = 1.72^{+0.04}_{-0.04}$. In the western lobe, we find $\Gamma_{0.5-2.0} = 1.80^{+0.19}_{-0.11}$ and $\Gamma_{2.0-7.0} = 1.94^{+0.25}_{-0.10}$. While the errors in the western lobe are too large to distinguish between these photon indices with any statistical certainty, the numbers are consistent with the possibility that we are indeed seeing a turnover in the non-thermal X-ray spectrum of the western lobe. Somewhat more surprising is that a similar effect is also observed in the eastern lobe, given that the photon index of $1.72^{+0.03}_{-0.03}$ agrees well with the radio data, and we do not expect the average photon index to be significantly lower than this. However, we note that our models are limited by the fact that each lobe and jet are modeled with only a single photon index. Therefore, the variation seen between the low and high energy bands on both sides should be taken as a sign that the true electron energy distributions are more complicated than assumed here.

The correlation plots in Appendix B provide further insight as to why the photon index in the west is higher. In the eastern lobe, the model shows a non-thermal surface brightness in region L1 that is clearly larger than in regions L2 and L3. This is consistent with the radio maps, which show more continuum emission closer towards the hotspots. By contrast, in the western lobe, L6 is not significantly brighter than regions L4 and L5. If the X-ray photon index follows the radio spectral index, we would expect it to be significantly higher closer towards the AGN. Therefore, the reason that the photon index in the western lobe is higher could be explained by the fact that L4 and L5 contribute more to the total flux in the west than L2 and L3 do in the east. Because these inner regions have a higher photon index, the average photon index for the entire lobe will also be higher.

This raises the question, what has caused the underlying discrepancy?. As we have discussed at the beginning of this section, it is possible that the environment in the lobes and jets itself is different, and that the turnover in the western side is at lower energies than on the eastern side. Additionally, Snios et al. (2018) have shown that the shock on the eastern side is stronger, and so the shock could have managed to create more energetic particles in region L1, pushing the average photon index in the eastern lobe to a lower value. A third possibility is that the geometrical assumptions

that we have made have influenced the results. In particular, the assumptions that link the normalisations of emission components between corresponding background, lobe and jet regions might be inaccurate, perhaps because the western lobe is less symmetric than the eastern lobe. This would cause too much or too little emission to be attributed to one of the emission components.

5.4   Contribution of infrared photons to the IC flux

In our analysis of the we have considered synchrotron and CMB photons as seed photons for the IC process. However, infrared photons emitted from the AGN and the dust around the AGN can additionally provide a significant contribution to the total IC flux (Brunetti et al. 1997). In this section, we estimate approximately how much these photons would contribute to the IC flux.

Weedman et al. (2012) calculate the strength of several IR spectral features in Cyg A, but do not provide a value for the total infrared luminosity L_{IR}. However, we have made use of the scaling relationship between $\nu L_\nu(7.8\,\mu m)$ and L_{IR}, which is $\log[L_{IR}/\nu L_\nu(7.8\,\mu m)] = 0.80 \pm 0.25$ in AGN with silicate absorption (Sargsyan et al. 2011). Using the value of $f_\nu(7.8\,\mu m) = 54$ mJy from Weedman et al. (2012) and using the upper limit of the scaling relationship, we find $L_{IR} \sim 1.8 \times 10^{45}$ erg s^{-1}. This is consistent with the scaling relationship between bolometric luminosity and infrared luminosity found in that same paper, using $L_{bol} \sim 3.8 \times 10^{45}$ erg s^{-1} from Privon et al. (2012).

We calculated the number density of infrared photons in the lobe as $N_{IR} = L_{IR}/(4\pi c d^2 E_{IR})$, where we have used $d = 40$ kpc as an average distance in the middle of the lobe, and $E_{IR} = 3.3 \times 10^{-14}$ erg ($\lambda_{IR} = 60\,\mu m$) as the characteristic energy of an infrared photon, corresponding to the peak of the SED (Privon et al. 2012). This yields $N_{IR} = 10$ cm^{-3}. Meanwhile, the energy density of the CMB is $u_{CMB} = 4.1 \times 10^{-13}(1 + z)^4$ erg cm^{-3} (Harris & Grindlay 1979), yielding a photon number density $N_{CMB} = 360$ cm^{-3}.

While the number density of CMB photons is larger, we also have to take into account that infrared photons have higher energy and therefore have access to a larger number of electrons to be inverse-Compton scattered to keV energies. A 60 μm photon requires $\gamma \sim 200$ to be upscattered to 1 keV, while a CMB photon requires $\gamma \sim 1000$ to be upscattered to 1 keV. Using the slope of the electron spectrum $p = 2.4$ in the eastern lobe, we find a relative electron number density of $N_{\gamma_{1000}}/N_{\gamma_{200}} = 0.11$. For the flux ratio at 1 keV of IC/CMB flux to infrared IC flux, we then estimate $f_{CMB}/f_{IR} \sim N_{CMB}N_{\gamma_{1000}}/N_{IR}N_{\gamma_{200}} = 4$.

The modelling in section 4.4 has shown that synchrotron radiation is the dominant component in both lobes, and that the CMB makes up between $10 - 50\%$ of the flux. If the IC/CMB flux is 4 times higher than the infrared IC flux, as our estimate indicates, the infrared IC flux would contribute 2.5 - 12.5% to the total IC flux.

We expect that including the infrared spectrum as an additional photon field in our model would reduce the pressures, as fewer electrons would be needed to produce the same X-ray flux. However, since the maximum contributions of the infrared photons are less than the errors in the pressures, including them in the model would not have significantly altered our results.

5.5   The X-ray jets as IC relic jets

MCMC sampling of the Bayesian models for the jets and lobes of Cyg A has yielded good constraints on their photon indices and flux densities. However, turning these into pressures introduces additional errors. The pressure is strongly dependent on the photon

index in particular, which leads to very large uncertainties, particularly in the western lobe. Additionally, it is not known what the radio spectrum of the relic jet would be. This has forced us to make assumptions about the shape of the spectrum.

The magnetic field strengths found in Table 8 are a factor of 2-6 below equipartition. This seems to be a typical value for FRII radio galaxies (Croston et al. 2005; Ineson et al. 2017). We compare the rim pressures with the IC pressure listed in Table 8 to constrain the particle content κ in the lobes. In the eastern lobe, the assumption of $\kappa = 0$ yields a pressure that is inconsistent with the rim pressure. Depending on the choice of γ_{min}, we require $1 < \kappa < 5$ in the eastern lobe to match the rim pressures. Croston & Hardcastle (2014) developed a model for FRI radio galaxies where jet entrainment of protons/ions could provide the necessary additional pressure. A similar process could also be at work here.

On the eastern side, if κ and γ_{min} in the jet have the same value as in the lobe, the lobe and jet pressure are the same within the errors. However, it is unclear what determines the particle content of the jet and how it is related to the particle content in the lobe. It is possible that κ in the jet is lower or higher than in the lobe. On the western side, the calculated jet and lobe pressures are the same within the errors as well, assuming the same κ and γ_{min}. At $\kappa = 0$ and $\gamma_{min} = 1$, both of these pressures are much higher than the western rim pressure. This would imply that $\kappa = 0$ and that γ_{min} is larger than in the eastern side. However, it is difficult to imagine a scenario where κ is significantly different between the eastern and western side. Given the discrepancy in photon indices, and the possibility of a turnover in the western side due to adiabatic losses or aging effects, we consider it more likely that we have overestimated the western lobe and jet pressures, as discussed in section 5.3.

Another possibility is that γ_{min} is higher than assumed in our analysis. A consequence of the steeper spectrum on the western side is that the pressure falls off more quickly with increasing γ_{min}. Therefore, if γ_{min} is higher on the western side than on the eastern side, it is possible to make the western lobe pressure consistent with the eastern lobe pressure.

We note that our relic jet model is significantly different from the pure IC/CMB jet with very low magnetic field, proposed by Steenbrugge et al. (2008). As already noted in Section 1, a problem of the IC/CMB jet model is that it requires a significantly higher electron density, which would result in much higher electron pressures in the jet. In our model, the magnetic field in the X-ray jet is lower than in the lobes by a factor of $\sim 35 - 65\%$. This allows for a higher electron density in the jet while still producing less synchrotron radiation than the lobe. At the same time, the magnetic field is still high enough that the produced synchrotron photons are energetic enough to be IC scattered to the keV energy range. In this way, SSC can be the dominant component of IC flux in the jet, and the electron density can be much lower than in a pure IC/CMB jet. However, it means that our model can only exist in a narrow region of parameter space. While the model shows how the X-ray jet could in principle exist as an IC relic, it raises the question of why the electron spectrum in the jet would have exactly this shape.

An additional complication of the relic jet model is the existence of jet knots. In modelling the jet pressures, we have assumed that the X-ray emission per unit volume is uniform throughout the jet. However, the deep *Chandra* exposure of the system reveals that there are several bright jet knots, most notably on the eastern side. We estimated the contrast of these brightness variations. We took the average counts per pixel in regions J1-J3, and subtracted the average counts per pixel from L1-L3. We find 40 counts per pixel on average in L1-L3, with a minimum of 5 and a maximum of 80

counts in a pixel. We repeated the procedure on the western side and found a pixel average of 15 counts, with minimum 0 and maximum 38 counts. This shows that there are significant brightness variations in both jets. This implies large variations in pressure along the jet.

To test the pressure variations in our model, we took one of the brightest parts of the eastern jet, in the middle of region J2. We defined a square region with the same width and orientation as the J2 jet region, and with a length of 4.5″centered on the brightest part. We then determined the background-subtracted average counts per pixel in this region to be 67 counts, or 1.67 times the average counts per pixel over the entire jet. We then ran *synch* for this region, using a flux density of 1.67 times higher than the flux density found in the eastern jet. The radio flux was scaled to the volume of the emitting region, but was not increased by a factor of 1.67, as the radio flux from the X-ray jet region is an upper limit. Modelling the jet knot in this way, we find pressures of $\sim 13 \times 10^{-10}$ erg cm^{-3} for $\gamma_{min} = 1$ or $\sim 6 \times 10^{-10}$ erg cm^{-3} for $\gamma_{min} = 10$. This narrows the range of parameters pressure balance with the surrounding lobe somewhat, especially given the fact that γ_{min} is likely to be low in the relic jet.

Unfortunately, the assumptions that we have made in trying to model the jet-like features are just too uncertain to be able to draw any definite conclusions about how whether the IC relic jet model is sustainable in Cyg A. While we find slightly higher pressures in the eastern jet compared to the lobe, both κ and γ_{min} are unknown quantities that can greatly influence the pressure in the relic jet.

Although we can not rule out an IC relic jet model based on the X-ray and radio spectra, it is unclear how these knots of bright emission in the X-ray jets could be maintained in the IC relic jet model, where the radio jets have expanded by a factor of a few from their original, rather narrow size. If the knots originate from the radio jet, and if the X-ray jet has reached pressure equilibrium with the surrounding lobe, the knots should have been smoothed out in the process.

6 CONCLUSION

Deep *Chandra* observations of the X-ray jets and lobes of Cyg A have allowed us to analyse the emission from these features in detail. In the lobes, we have used two different tests to compare thermal and non-thermal models. In both lobes, we find that spectral fits strongly prefer a model with a non-thermal emission component for the lobe emission. In the X-ray jets, we used the thermal and non-thermal components of the ICM and lobe emission, and compared between a model with an additional thermal or additional non-thermal component for the jet emission. We find that the model with a non-thermal component for the jet is moderately to strongly preferred.

MCMC sampling of the non-thermal lobe and jet models has given us constraints on the flux and photon indices of the jets and lobes. For the eastern lobe and jet, we find 1 keV flux densities of 71^{+10}_{-10} nJy and 24^{+4}_{-4} nJy, and photon indices of $1.72^{+0.03}_{-0.03}$ and $1.64^{+0.04}_{-0.04}$ respectively. For the western lobe and jet, we find flux densities of 50^{+12}_{-13} nJy and 13^{+5}_{-5} nJy, and photon indices of $1.97^{+0.23}_{-0.10}$ and $1.86^{+0.18}_{-0.12}$ respectively.

For each lobe, we used broken power laws with an age break to model the electron energy distributions. A comparison with the rim pressures from Snios et al. (2018) shows that a significant population of non-radiating particles is required to account for the total pressure of the eastern lobe. We also find a magnetic field of around 40 μG, a factor 2 lower than the equipartition value of $73 - 95$ μG . This ratio

of B/B_{eq} agrees well with a sample of other FRII radio galaxies (Ineson et al. 2017).

However, in the western lobe no population of non-radiating particles is required and the low energy cutoff of the electron distribution needs to be raised to obtain a pressure consistent with the rim pressure. This discrepancy is a consequence of the difference in photon index between the two lobes, and suggests that the true electron distributions may be more complex than a single broken power law. A possible cause for the discrepancy is that the SSC component of the spectrum in the western lobe could have a turnover at lower energies than in the eastern lobe, perhaps because of the difference in size. A spectral turnover below a few keV would yield a higher photon index in the $0.5 - 7.0$ keV energy range. The data are slightly suggestive of a turnover in this range, with a lower photon index between $0.5 - 2.0$ keV than at $2.0 - 7.0$ keV, although the constraints are not strong. A further complicating factor is the fact that the photon index likely isn't constant throughout the lobe. The correlation plots in Appendix B show that the inner regions on the western side (L4 and L5) contribute more to the total flux than the inner regions on the eastern side (L2 and L3). Because these regions presumably have a higher photon index, the average photon index for the western lobe will be higher as well.

Regardless of the cause, if the photon index in the western lobe is overestimated, then the pressures on that side are overestimated as well. We consider the photon index in the eastern lobe more likely to be accurate because it agrees well with values in the literature of the average radio spectral index in the lobes.

We modeled the X-ray jets according to the IC relic jet model from Steenbrugge et al. (2008). Similar to the lobes, we used the X-ray and radio data to constrain the spectra and model the electron distributions. On the 150 MHz LOFAR data, a weak brightness enhancement is seen at roughly the location of the relic jet, although imperfectly aligned. This could indicate the presence of the IC relic jet in radio wavelengths, but the emission is too weak to be able to constrain the radio synchrotron spectrum. Therefore, assumptions have to be made about the normalisation of the radio frequency and the break frequency. Moreover, $\gamma_{\min}$ and κ are poorly constrained, making the modelling uncertain.

We find a higher median pressure in the eastern jet compared to the lobe, but still within the errors. This suggests that an IC relic jet could be relatively close to pressure balance with the surrounding lobe. However, the IC relic jet model as we have modeled it can only exist in the narrow region of parameter space. The magnetic field needs to be lower than in the lobe, so that the jet is not brighter than the lobe in the radio. At the same time, if the IC flux is dominated by SSC, the magnetic field needs to be high enough to produce synchrotron photons that can be scattered to the kev energy range.

An additional problem is that the model does not take into account the jet knots of increased brightness. If these knots originate from the radio jet, we would expect them to have been smoothed out in the process of adiabatic expansion if the current jet is close to achieving pressure balance with the lobe. Better constraints on the synchrotron spectrum, and more detailed modelling to allow for variations in flux and photon index along the jet axis, will be needed to shed more light on the nature of the jet-like X-ray features in Cyg A.

ACKNOWLEDGEMENTS

REFERENCES

Anders E., Grevesse N., 1989, Geochimica Cosmochimica Acta, 53, 197
Bartalucci I., Mazzotta P., Bourdin H., Vikhlinin A., 2014, A&A, 566, A25
Bîrzan L., Rafferty D., McNamara B., 2004, ApJ, 607, 800
Brunetti G., Setti G., Comastri A., 1997, A&A, 325, 898
Carilli C. L., Perley R. A., Dreher J. H., 1988, ApJ, 334, L73
Carilli C. L., Perley R. A., Dreher J. W., Leahy J. P., 1991, ApJ, 383, 554
Carilli C. L., Perley R. A., Harris D. E., 1994, MNRAS, 270, 173
Celotti A., Ghisellini G., Chiaberge M., 2001, MNRAS, 321, L1
Chon G., Böhringer H., Krause M., Trümper J., 2012, A&A, 545, L3
Croston J. H., Hardcastle M. J., 2014, MNRAS, 438, 3310
Croston J., Hardcastle M., Harris D., Belsole E., Birkinshaw M., Worrall D., 2005, ApJ, 626, 733
Croston J. H., Hardcastle M. J., Birkinshaw M., Worrall D. M., Laing R. A., 2008, MNRAS, 386, 1709
Dickey J. M., Lockman F. J., 1990, ARA&A, 28, 215
Dreher J., Carilli C., Perley R., 1987, ApJ, 316, 611
Duffy R. T., et al., 2018, MNRAS,
Fanaroff B., Riley J., 1974, MNRAS, 167, 31
Foreman-Mackey D., Hogg D. W., Lang D., Goodman J., 2013, PASP, 125, 306
Freeman P., Doe S., Siemiginowska A., 2001, in Starck J.-L., Murtagh F. D., eds, Proc. SPIEVol. 4477, Astronomical Data Analysis. pp 76–87 (arXiv:astro-ph/0108426), doi:10.1117/12.447161
Fruscione A., et al., 2006, in Society of Photo-Optical Instrumentation Engineers (SPIE) Conference Series. p. 62701V, doi:10.1117/12.671760
Gelman A., 2006, Bayesian Analysis, 1, 1
Goodman J., Weare J., 2010, Comm. App. Math. Comp. Sci, 5, 65
Hardcastle M., 2006, MNRAS, 366
Hardcastle M., Croston J., 2010, MNRAS, 404, 2018
Hardcastle M. J., Birkinshaw M., Worrall D. M., 1998, MNRAS, 294, 615
Hardcastle M. J., Worrall D. M., Birkinshaw M., Laing R. A., Bridle A. H., 2002, MNRAS, 334, 182
Hardcastle M. J., Kraft R. P., Worrall D. M., Croston J. H., Evans D. A., Birkinshaw M., Murray S. S., 2007, ApJ, 662, 166
Hardcastle M., et al., 2016, MNRAS, 455, 3526
Harris D. E., Grindlay J. E., 1979, MNRAS, 188, 25
Hickox R. C., Markevitch M., 2006, ApJ, 645, 95
Hinshaw G., et al., 2013, ApJS, 208, 19
Ineson J., Croston J. H., Hardcastle M. J., Mingo B., 2017, MNRAS,
Jester S., Harris D. E., Marshall H. L., Meisenheimer K., 2006, ApJ, 648, 900
Kalberla P. M. W., Burton W. B., Hartmann D., Arnal E. M., Bajaja E., Morras R., Pöppel W. G. L., 2005, A&A, 440, 775
Konar C., Hardcastle M. J., Croston J. H., Saikia D. J., 2009, MNRAS, 400, 480
Mazzotta P., Rasia E., Moscardini L., Tormen G., 2004, MNRAS, 354, 10
McKean J. P., et al., 2016, MNRAS, 463, 3143
Morganti R., Fanti R., Gioia I. M., Harris D. E., Parma P., de Ruiter H., 1988, A&A, 189, 11
Perley R. A., Dreher J. W., Cowan J. J., 1984, ApJ, 285, L35
Polson N. G., Scott J. G., 2011, preprint, (arXiv:1104.4937)
Privon G. C., Baum S. A., O'Dea C. P., Gallimore J., Noel-Storr J., Axon D. J., Robinson A., 2012, ApJ, 747, 46
Sargsyan L., Weedman D., Lebouteiller V., Houck J., Barry D., Hovhannisyan A., Mickaelian A., 2011, ApJ, 730, 19

Schwartz D. A., et al., 2006, ApJ, 647, L107

Smith R., Brickhouse N., Liedahl D., Raymond J., 2001, ApJ, 556, L91

Snios B., et al., 2018, ApJ, 855, 71

Spinrad H., Marr J., Aguilar L., Djorgovski S., 1985, PASP, 97, 932

Steenbrugge K., Blundell K., 2008, MNRAS, 388, 1457

Steenbrugge K., Blundell K., Duffy P., 2008, MNRAS, 388, 1465

Stockton A., Ridgway S., 1996, in Carilli C. L., Harris D. E., eds, Cygnus A – Study of a Radio Galaxy. p. 1

Stockton A., Ridgway S. E., Lilly S. J., 1994, AJ, 108, 414

Tavecchio F., Maraschi L., Sambruna R. M., Urry C. M., 2000, ApJ, 544, L23

Thiébaux H. J., Zwiers F. W., 1984, Journal of Applied Meteorology, 23, 800

Uchiyama Y., et al., 2006, ApJ, 648, 910

Vestergaard M., Barthel P. D., 1993, AJ, 105, 456

Weedman D., Sargsyan L., Lebouteiller V., Houck J., Barry D., 2012, ApJ, 761, 184

Wilson A., Smith D., Young A., 2006, ApJ, 644, L9

Yaji Y., Tashiro M., Isobe N., Kino M., Asada K., Nagai H., Koyama S., Kusunose M., 2010, ApJ, 714, 37

APPENDIX A: STATISTICAL TOOLS

A1 Bayesian inference

Bayesian inference is based on Bayes' theorem,

$$p(\Theta|\mathbf{D}, M) = \frac{p(\mathbf{D}|\Theta, M)p(\Theta|M)}{p(\mathbf{D}|M)}. \tag{A1}$$

We compare a data set, $\mathbf{D}$, with a model M, which contains a set of parameters $\Theta = \{\Theta_1, \Theta_2......\Theta_N\}$. $p(\Theta|\mathbf{D}, M)$ is referred to as the *posterior*. $p(\mathbf{D}|\Theta, M)$ is the probability of the data given parameters Θ and model M, and is referred to as the *likelihood*. $p(\Theta|M)$ encodes our prior knowledge of the system and is called the *prior*. The normalising constant, $p(\mathbf{D}|M)$ is called the *marginal likelihood*, and is the product of the likelihood and the prior integrated over the entire parameter space. The marginal likelihood is an important quantity in model selection and can be used to calculate the relative odds of two different models. However, calculating the marginal likelihood is computationally expensive for a model with a large number of parameters. Therefore we use unnormalised posteriors.

For computational convenience, we take the natural log of Eq. A1. This allows us to sum the log terms of the equation. We will refer to the log terms as loglikelihood, logprior and logposterior.

The data set $\mathbf{D}$ consists of data points D_{ij} for spectrum i and spectral bin j, with a total of N spectra and J spectral bins per spectrum. The likelihood of the data, given M with parameters Θ, is the Poisson distribution multiplied over each bin of the data set,

$$L(\Theta) = \prod_{i=0}^{N} \prod_{j=0}^{J} \left\{ \frac{e^{-m(\Theta)} m(\Theta)^{D_{ij}}}{D_{ij}!} \right\} \tag{A2}$$

By taking the log of this equation, we obtain the Poisson loglikelihood,

$$\log(L(\Theta)) = \sum_{i=0}^{N} \sum_{j=0}^{J} \left\{ -m(\Theta) + D_{ij} \log(m(\Theta)) - \log(D_{ij}!) \right\} \tag{A3}$$

A *Maximum Likelihood Estimation*, or MLE, estimates the most likely parameters $\hat{\Theta}$ by finding the parameters that maximise the likelihood. The Bayesian equivalent to a MLE is called a *Maximum A Posteriori estimation*, or MAP. It is the set of parameters that maximises the posterior,

$$\hat{\Theta}_{\text{MAP}} = \arg \max_{\Theta} (p(d|\Theta, M)p(\Theta|M)) \tag{A4}$$

Table A1. The Jeffreys scale.

$\Delta AIC/\Delta BIC$	Odds	Probability	Strength of evidence
<1.0	$\lesssim$ 3:1	0.750	Inconclusive
1.0	$\sim$ 3:1	0.750	Positive evidence
2.5	$\sim$ 12:1	0.923	Moderate evidence
5.0	$\sim$ 150:1	0.993	Strong evidence

The MAP is a useful tool to find the area of maximum likelihood. This is useful, both for the model selection tests as well as to provide starting parameters for MCMC.

A2 Markov Chain Monte Carlo sampling

In problems with large numbers of parameters, the posterior can become a highly complicated function. This is why we use Markov Chain Monte Carlo (MCMC) to sample the posterior. MCMC generates random samples of parameters by moving through the parameter space with Markov chains. Provided that these chains converge in a certain region of parameter space, the sampled parameter sets will the posterior distribution of the parameters.

We used the Python module *emcee* of Foreman-Mackey et al. (2013) which implements an affine invariant ensemble MCMC sampler based on Goodman & Weare (2010). The initial parameters for each of the chains are generated by a normal distribution centred on the MAP estimate for that parameter set.

The output of MCMC is a large set of sampled parameters for the given model. Because we assume that the MCMC sampling maps the posterior function, these samples show us the values each parameter can have, and the likelihoods of these values. The MCMC sampled distribution of a parameter is therefore referred to as a a *posterior distribution*.

A3 Model selection methods

A3.1 Akaike/Bayesian information criterion

The most important quantity in Bayesian model selection is the Bayes factor, also called the *evidence*. The evidence is the ratio of marginal likelihoods of the models. If we consider Bayes' theorem for a model M_i, it is written as

$$p(M_i|\mathbf{D}) \propto p(\mathbf{D}|M_i)p(M_i). \tag{A5}$$

If we now assume that the priors for both models are equal: $p(M_0) = p(M_1) = 0.5$, we can write

$$B_{01} = \frac{p(M_1|\mathbf{D})}{p(M_0|\mathbf{D})} = \frac{p(\mathbf{D}|M_1)}{p(\mathbf{D}|M_0)}. \tag{A6}$$

Therefore, the ratio of marginal likelihoods of two models is equal to the ratio of the likelihood of the models. Because the marginal likelihood is difficult and computationally expensive to compute, we often use approximations. The Akaike Information Criterion (AIC, eq. A7) (**?**), and the Bayesian Information Criterion (BIC, eq. A8) (**?**), are two such approximations that approach the marginal likelihood under certain circumstances.

AIC and BIC include two terms: one for the *complexity* of the model and one for the *likelihood*. These terms have opposite signs. A model with more parameters will always be able to give a higher likelihood in a fit, but adding 'unnecessary' extra parameters will

result in overfitting. Therefore the best model is the one that has the highest likelihood while being the least complex.

The AIC is defined as

$$AIC = 2k - 2\ln\hat{L} \qquad (A7)$$

and the BIC as

$$BIC = \ln(n)k - 2\ln\hat{L}, \qquad (A8)$$

where k is the number of free parameters in the model, $\hat{L}$ is the maximum likelihood of the model fit to the data, and n the number of independent data points. Eqs A7 and A8 differ only in the first term. Because most of the time $\ln(n)k > 2k$, the BIC prefers less complex models more strongly.

The model with the lowest AIC or BIC is considered the most likely model. The relative odds of two models can be calculated from the difference in AIC/BIC values. The scale of relative odds between two models is known as the Jeffreys Scale (**???**). An example of $\Delta AIC/\Delta BIC$ and corresponding relative odds is shown in Table A1 (taken from **?**).

The AIC assumes a large sample size. For smaller sample sizes, a correction needs to be applied. This is called the corrected AIC or, AIC_C (**?**)

$$AIC_C = 2k - 2\ln\hat{L} + \frac{2(k+1)(k+2)}{n-k-2}. \qquad (A9)$$

While AIC and BIC are widely-used in model selection, they also have certain disadvantages. They depend only on the maximum likelihood, which means the prior information is not considered. Secondly, a model with degenerate, and therefore unconstrained, parameters will be overly penalised by AIC and BIC : the model complexity increases with little gain to the goodness-of-fit. The number of free parameters is therefore not necessarily a good indication of model complexity (**?**).

A3.2 Likelihood-ratio test

The likelihood ratio test is a form of hypothesis testing for nested models. We form our null hypothesis, $H_0 : M = M_0$, and the alternative hypothesis, $H_1 : M = M_1$. We define the Likelihood-ratio test statistic, T_{LRT}, as:

$$T_{LRT} = \ln\left(\frac{p(\mathbf{D}|\hat{\Theta}_1, M_1)}{p(\mathbf{D}|\hat{\Theta}_0, M_0)}\right) \qquad (A10)$$

We find the likelihood ratio of models M_1 and M_0 by determining the likelihood which corresponds to the MAP estimate for each model. Assuming H_0, we want to find out where the likelihood ratio lies on the distribution of possible likelihood ratios between M_1 and M_0. If the observed ratio lies in the tail of the likelihood ratio distribution, it would be very unlikely to occur by chance under the null hypothesis. By comparing the T_{LRT} with the distribution of likelihood ratios, we can decide whether we have cause to reject M_0 or not.

The downside of hypothesis testing is that the p-value tells us the probability that we can reject M_0. It does not say anything about the likelihood of M_1.

To obtain a distribution of possible likelihood ratios, we need predictive data assuming the null hypothesis. We MCMC sampled model M_0 for the eastern and western lobe. The MCMC sampling was done in as described in section A2. We then picked a random parameter set from the sample and generated a fake spectrum with the Sherpa tool *fake_pha*. This fake spectrum is effectively a simulated future observation of the data, assuming H_0. We again find the likelihoods corresponding to the MAP estimates for model M_0 and M_1 to the simulated spectrum and calculate the likelihood ratio. By drawing repeated samples, generating fake data, and calculating the likelihood ratio, we obtain a likelihood ratio distribution to which we can compare the likelihood ratio of the real data. From this we can calculate the p-value.

APPENDIX B: CORRELATION PLOTS

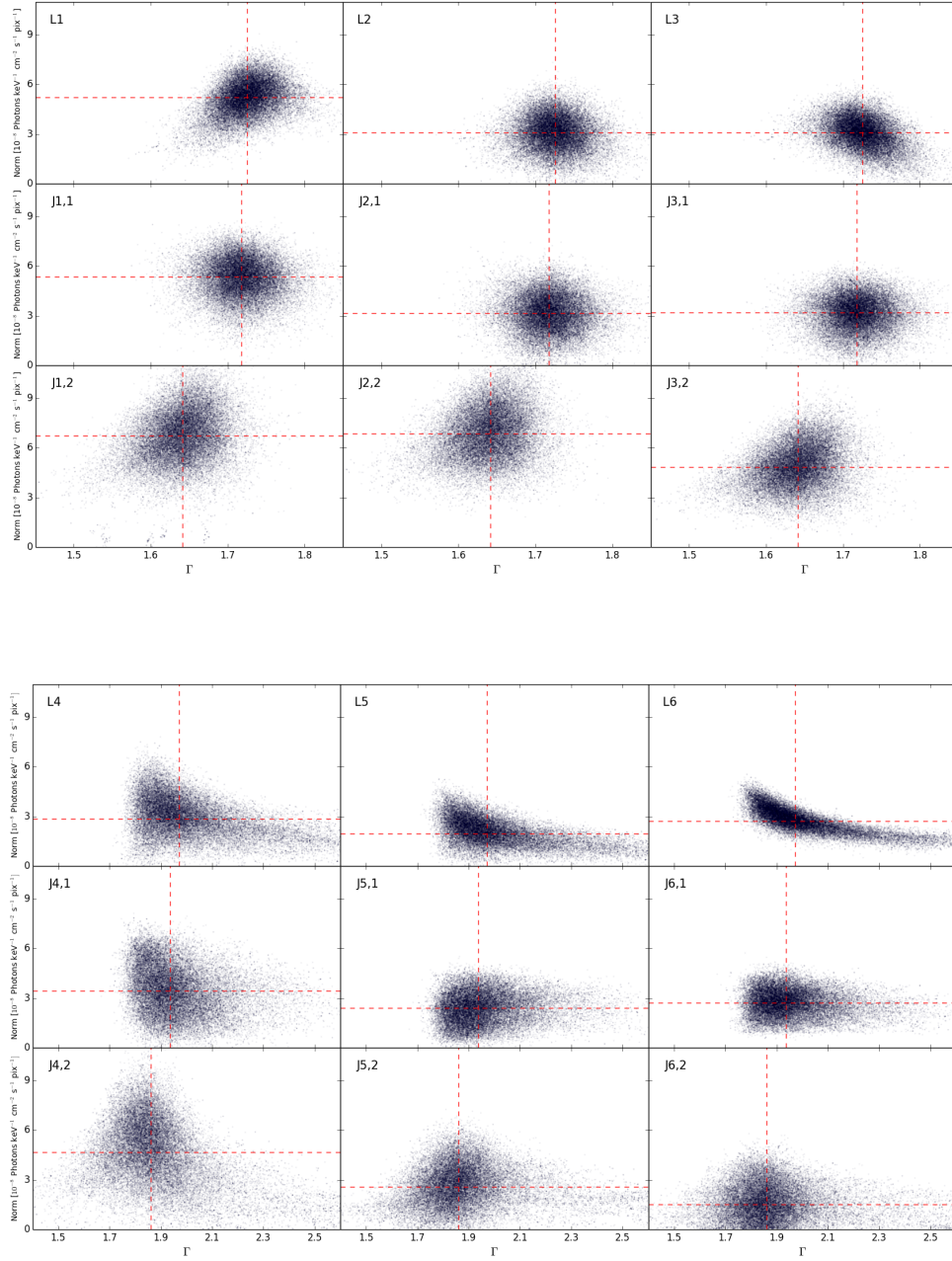This paper has been typeset from a TEX/LATEX file prepared by the author.

Figure B1. Top: Scatter plots that show the correlation between Γ and surface brightness for each non-thermal emission component in each region of the eastern lobe. The surface brightness is expressed as the spectral normalisation of the APEC model divided by the pixel area of the region. The dashed horizontal and vertical red lines indicate the median normalisations and photon indices respectively. The labels in the top left indicate the region. In the jet regions the emission component is additionally specified. I.e. J1,1 indicates the non-thermal emission from the lobe in region J1. Bottom: As above, for the western lobe.